

Linearized General Relativity in hyperboloidal slices

Inês Andrade Rainho

Thesis to obtain the Master of Science Degree in

Physics Engineering

Supervisors: Prof. David Hilditch
Dr. Alex Vañó-Viñuales
M.Sc. Christian Peterson Bórquez

October 2022

A ti, que partes com o coração nas mãos e as lágrimas nos olhos, a ansiedade de chegar onde o coração pertence e as lágrimas desaguam, Estás agora mais perto do destino que escolheste, mas a viagem ainda é longa. Apertas no peito a saudade que no peito te aperta e na melodia do vento afogas o pensamento, agora quase vazio. Reconheces no silêncio do autocarro a ausência daqueles cujo itinerário eleito foi outro. Em breve, acolher-te-á o colo quente dos que sempre esperam ansiosamente ver-te chegar uma vez mais. Eles saberão cuidar de ti. Sempre souberam.

Aos meus pais, por esta vida linda.

Acknowledgments

I am incredibly grateful to my supervisors, David, Alex, and Christian, who warmly welcomed me to work with them. They showed me how exciting it can be to do science and taught me to think critically about my and others' work. David spent endless hours clarifying all my doubts and would always make time for at least a five minutes discussion, even when his schedule was full. He can make the most complex problems seem simple and their resolution logical and straightforward. David is not only a great teacher but also a good friend. He, above all people, encouraged me to pursue a career in science and inspired me to do so, even indirectly, by manifesting his admiration for a female physicist. I am thankful for all the Mathematica tips and tricks that Alex shared with me and for teaching me to express my ideas with scientific rigor. I truly appreciate his attentiveness in sharing useful information, from job posts to workshops and classes I might have been interested in, and for his advice and guidance. I want to thank Christian for his patience, support, and friendship. It is always a delight working with him. I am beyond grateful for everything he taught me, for every minute spent together fighting with the code, and for the friendship that blossomed from there. It feels surreal to connect with someone born and raised across the Atlantic. *Gracias, amigo.*

I would also like to thank the other GRIT members for welcoming me. I feel lucky I got to be a part of such a nice group.

I acknowledge financial aid from *Serviços de Ação Social da Universidade de Lisboa*, *Associação Duarte Tarré*, and *Fundação Calouste Gulbenkian*, without which I would not be standing here today.

A special thanks to my childhood friend Vânia, who still manages to be a part of my life albeit living across the globe. To my colleagues and friends, who helped me get through the last five years, António, Carolina, Dinis, Filipa, Henrique Borges, João Gonçalves, João Santos, Maria Mesquita, Nuno Olavo, Sérgio, Zeca – my sincere thanks, I learned a lot from all of you. Félix, Iara, and Mariana Brejo, thank you for making this journey brighter.

I am thankful for my siblings, who have read this entire document despite them not having the background to understand most of it. Raquel, I will always look up to you. David, I hope I can continue to annoy you for decades to come. I love you both.

Miguel, my best friend, you inspire me to be better every day. Thank you.

Lastly, I thank my parents for their unconditional love and support and for everything they sacrificed to ensure I had the best education possible. To my dad, who always believed I could be anything I wanted, and to my mom, my wonder-woman, the most loving and hard-working person I know, *obrigada*. You may not hold PhDs, but you were the ones who taught me the most, who taught me what equations cannot model.

Abstract

The treatment of future null infinity in Numerical Relativity is still an open problem. Its relevance is due to it being the only location in spacetime where gravitational radiation can be unambiguously measured, and is also the appropriate idealization of observers of astrophysical events. The accuracy of the waveforms extracted from numerical simulations is crucial to estimate the correct properties of the sources of gravitational radiation observed by the interferometers. Currently, these waveforms are computed by either extrapolation or Cauchy-characteristic extraction/evolution. However, these methods are unsatisfactory from a first principles perspective. In this work, we take an alternative approach – the hyperboloidal method – in which spacetime is foliated into spacelike hypersurfaces that reach future null infinity. To do that, we introduce new coordinates that compactify spacetime. In these coordinates, the wave equations have formally singular terms, which we can overcome by considering the rate of decay of the fields and rescaling them such that the equations become regular at future null infinity. To better understand the rate of decay of the fields, we introduce the good-ugly model and show that it reproduces the behavior of the linearized Einstein equations. We implement the hyperboloidal approach for the model equations and show that they are regular at future null infinity. For the numerical implementation, we use the NRPy+ code and solve the equations in first-order in time and space with axially symmetric initial data on a staggered grid. Clean convergence is found, indicating a successful result. A similar approach can be done for full General Relativity, albeit with additional complications.

Keywords

Compactification; Future null infinity; General Relativity; Gravitational wave astronomy; Hyperboloidal; Numerical Relativity.

Resumo

O tratamento do infinito nulo futuro na Relatividade Numérica é ainda um problema em aberto. A sua relevância deve-se ao facto de ser o único “local” no espaço-tempo onde a radiação gravitacional pode ser medida de forma inequívoca, e de corresponder também à idealização adequada de observadores de eventos astrofísicos. A precisão das formas de onda extraídas das simulações numéricas é crucial para estimar a correta propriedades das fontes de radiação gravitacional observadas pelos interferómetros. Atualmente, essas formas de onda são calculadas por extrapolação ou por extração/evolução Cauchy-característica. No entanto, esses métodos são insatisfatórios do ponto de vista de primeiros princípios. Neste trabalho, adotamos uma abordagem alternativa – o método hiperboloidal –, em que o espaço-tempo é foliado em hipersuperfícies espaciais que se estendem até ao infinito nulo futuro. Para isso, introduzimos novas coordenadas que compactificam o espaço-tempo. Nestas coordenadas, as equações de onda têm termos formalmente singulares, o que podemos superar considerando a taxa de decaimento dos campos e redimensionando-os tal que as equações se tornem regulares no infinito nulo futuro. Para entender melhor a taxa de decaimento dos campos, apresentamos o modelo *good-ugly* e mostramos que reproduz o comportamento das equações linearizadas de Einstein. Implementamos a abordagem hiperboloidal para as equações do modelo e mostramos que elas são regulares no infinito nulo futuro. Para a implementação numérica, usamos o código NRPy+, e resolvemos as equações em primeira ordem no tempo e no espaço com dados iniciais axialmente simétricos numa grelha que não inclui os extremos. Verifica-se convergência, indicando um resultado bem-sucedido. Uma abordagem semelhante pode ser feita para a Relatividade Geral completa, embora

com complicações adicionais.

Palavras Chave

Astronomia de ondas gravitacionais; Compactificação; Hiperboloidal; Infinito nulo futuro; Relatividade Geral; Relatividade numérica.

Contents

1	Introduction	1
2	Gravitational Waves	5
2.1	Brief Review of General Relativity	7
2.1.1	Introduction	7
2.1.2	Curved spacetime	7
2.2	Linearized Theory	8
2.2.1	Expansion around flat space	8
2.2.2	Gauge freedom	9
2.2.3	The Transverse-Traceless gauge	11
2.2.3.A	Physical intuition of the propagating degrees of freedom	12
3	Approaches to the weak-field regime in Numerical Relativity	15
3.1	Wave extraction, Cauchy-Characteristic matching, and extraction	16
3.2	Hyperboloidal compactification	18
3.3	Conformal formalism	19
3.4	The good-bad-ugly model	21
4	Numerical methods	23
4.1	Finite differences	24
4.2	Method of Lines	25
4.3	Convergence testing	26
5	Gravitational Waves in Hyperboloidal Slices	29
5.1	Geometric Setup	30
5.1.1	Geometric quantities	30
5.1.2	Linearization	31
5.2	Regularization at the origin	32
5.3	Regularization at future null infinity	35
5.4	Model equations	38
5.4.1	Generalized Harmonic Gauge	38

5.4.2	Transverse-Traceless gauge	41
6	Numerical simulations	43
6.1	NRPy+	44
6.2	Implemented equations	44
6.3	Boundary Condititons	45
6.4	Numerical treatment of the origin	47
6.5	Initial Data	47
6.6	Results	48
7	Discussion of the results	53
7.1	Summary	54
7.2	Future work	54
	Bibliography	57
A	Geometric quantities	61
B	Source terms in the GU model	65

List of Figures

2.1	Representation of how a set of pointlike particles initially distributed in a circle are perturbed by a Gravitational Wave (GW) traveling perpendicularly to them when $H_{\times} = 0$. . .	12
2.2	Representation of how a set of pointlike particles initially distributed in a circle are perturbed by a GW traveling perpendicularly to them when $H_{+} = 0$	13
3.1	Penrose diagram of Minkowski spacetime foliated along Cauchy and characteristic slices.	17
3.2	Penrose diagram of Minkowski spacetime foliated along hyperboloidal slices.	20
4.1	Representation of the computational grid.	24
6.1	Dynamics of the evolution of the G (on top) and U (on the bottom panel) fields in axial symmetry starting with initial data given in Sec. 6.5. The evolution depicted here was performed with 120 grid points in the radial coordinate, 24 grid points in θ , and 4 points in ϕ . Even though we are evolving axially symmetric data, four points in ϕ are needed for the boundary conditions, which have two ghost zones. As expected, the <i>ugly</i> fields decay must faster than the <i>goods</i> , and are always zero at future null infinity.	49
6.2	Dynamics of the evolution of the G_{θ} (on top) and U_{θ} (on the bottom panel) fields in axial symmetry starting with initial data according to Sec. 6.5. The evolution depicted here was performed with 120 grid points in the radial coordinate, 24 grid points in θ , and 4 points in ϕ . Although we are taking an axially symmetric expression for the initial data, we use 4 points in ϕ . Even though we are evolving axially symmetric data, four points in ϕ are needed for the boundary conditions, which have two ghost zones. As expected, the <i>ugly</i> fields decay must faster than the <i>goods</i> , and are always zero at future null infinity.	50

6.3	Values of the (a) G , (b) G^- , and (c) G_θ fields at \mathcal{I}^+ for all values of time and θ from the evolution with 80 grid points in r , 16 in θ and 4 in ϕ starting with initial data according to Sec. 6.5. Even though we are evolving axially symmetric data, four points in ϕ are needed for the boundary conditions, which have two ghost zones. The values were obtained through a fourth-order extrapolation, necessary due to the centered grid. We notice that for later times the fields vanish, indicating that the signals leave the domain completely through \mathcal{I}^+	51
6.4	Norm convergence of the state-vector $(G, G^+, G^-, G^\theta, U, U^+, U^-, U^\theta)$ in axial symmetry with the norm (6.19), starting with 80 grid points in r , 16 in θ and 4 in ϕ and increasing the resolution by a factor of $p = 1.5$. Even though we are evolving axially symmetric data, four points in ϕ are needed for the boundary conditions, which have two ghost zones. We see that the convergence factor approaches 2, as anticipated for second-order finite differences approximation, which indicates a successful result.	51
6.5	Rescaled differences at \mathcal{I}^+ with $\theta = 0.5$ for: (a) the G field, (b) the G^- field, and (c) the G_θ field. Starting with 80 grid points in the radial coordinate, 16 in θ and 4 in ϕ , the resolution was increased by a factor of $p = 1.5$. Even though we are evolving axially symmetric data, four points in ϕ are needed for the boundary conditions, which have two ghost zones. The evolution was performed with second-order finite differencing approximation of spatial derivatives, i.e. $n = 2$. l, m, and h stand for the values of the corresponding field given by the low, medium, and high-resolution runs, respectively. The alignment of the rescaled differences indicates convergence at \mathcal{I}^+	52

Acronyms

BH	Black Hole
CCE	Cauchy-Characteristic extraction/evolution
CCM	Cauchy-Characteristic matching
EFE	Einstein field equations
EM	electromagnetic
EOM	Equation of Motion
GBU	good-bad-ugly
GU	good-ugly
GHG	Generalized Harmonic Gauge
GR	General Relativity
GW	Gravitational Wave
IVP	Initial Value Problem
IBVP	Initial Boundary Value Problem
LIGO	Laser Interferometer Gravitational-Wave Observatory
MOL	Method of Lines
NR	Numerical Relativity
ODE	Ordinary Differential Equation
PDE	partial differential equation
RHS	right-hand side
RK4	fourth-order Runge-Kutta
TT	Transverse-Traceless
tt	transverse-traceless

1

Introduction

General Relativity (GR) has been the most successful theory of gravity since its postulation. It predicts the existence of Gravitational Waves (GWs), which were directly detected for the first time in 2015 by the Laser Interferometer Gravitational-Wave Observatory (LIGO) [1, 2]. Since then, GWs have been detected frequently, and have brought with them information about the universe. These detections gave very strong evidence for the existence of Black Holes (BHs), and, along with their electromagnetic counterpart, imposed constraints on modified theories of gravity [3].

The data gathered by GW detectors is compared with waveforms obtained from numerical simulations to look for a gravitational wave signal. Thus, the precision of the theoretical waveforms is critical for recovering the correct properties of the systems that emitted the signal. In Numerical Relativity (NR), these waveforms are obtained by evolving the system (usually a coalescing compact binary) using the Einstein field equations (EFE) and extracting the emitted signals. Gravitational radiation is only unambiguously defined at future null infinity (\mathcal{I}^+), the “location” in spacetimes where light rays arrive, and which also corresponds to the correct idealization of astrophysical observers. Currently, waveforms are obtained at future null infinity by either extrapolation or using Cauchy-Characteristic extraction/evolution (CCE). The most common way is to compute the relevant quantities at several radii and perform an extrapolation to future null infinity. In CCE, spacetime is divided into a Cauchy and a characteristic domain reaching null infinity, separated by an unphysical boundary. The characteristic domain uses as initial data the evolution from the Cauchy domain and allows us to reach future null infinity. However, this method poses some problems, namely if we evolve for a longer period of time the waveform gets affected by the unphysical boundary. This is not satisfactory from a first principles viewpoint.

The use of hyperboloidal slices is a possible solution to this problem. Hyperboloidal slices are space-like and smooth everywhere, and by definition, they reach future null infinity, which allows us to unambiguously extract gravitational waves. In practice, evolving on hyperboloidal slices requires writing the EFE in a new set of coordinates adapted to outgoing waves. By performing this coordinate transformation, infinity is brought to a finite coordinate distance. This introduces infinities in the equations themselves, but they can be overcome by considering the rate of decay of the fields as we approach future null infinity. In this process, we sacrifice the signals coming from future null infinity. However, this is not to worry about, since an accurate computation of gravitational radiation can only be done in a neighborhood of \mathcal{I}^+ .

The thesis is structured as follows: In chapter 2, we review the most important aspects of GR and explain how GWs emerge from GR. In chapter 3, we give a brief description of the methods used to extract gravitational radiation at future null infinity and introduce the approach taken in this work. In chapter 4, we explain important methods used in NR. We focus, in particular, on the ones used in this project. The geometric setup of this work is given in chapter 5. A careful regularization at the origin and future null infinity is done, and the linearized EFE are derived. Then, we show that these equations

can be modeled by two types of equations. The details of the numerical implementation are given in chapter 6, as well as the results obtained. Finally, in chapter 7, we discuss the importance of this work and explore how it can be continued.

2

Gravitational Waves

Contents

2.1	Brief Review of General Relativity	7
2.2	Linearized Theory	8

GR predicts the existence of ripples in spacetime that propagate at the speed of light – called gravitational waves. GWs are the propagating degrees of freedom that are manifest in the curvature. Analogously to electromagnetism, where electromagnetic waves are generated by moving charges, in GR gravitational waves are generated by moving masses. However, the power emitted by gravitational radiation scales as

$$\mathcal{P} = \frac{G}{5} \ddot{Q}_{ij} \ddot{Q}^{ij}, \quad (2.1)$$

where $G = 6.67 \times 10^{-11} \text{ m}^3 \text{kg}^{-1} \text{s}^{-2}$ is Newton's gravitational constant, and Q_{ij} is the traceless part of the quadrupole moment

$$I_{ij}(t) = \int_{\Sigma} d^3x T^{00}(\mathbf{x}, t) x_i x_j \quad (2.2)$$

evaluated in retarded time $u = t - r$. In the regime where Newtonian gravity is a good approximation, the quadrupole moment of the energy emitted by two masses M at a distance R orbiting around each other is

$$I_{ij}(t) = \frac{MR^2}{4} \begin{pmatrix} 1 + \cos 2\omega t & \sin 2\omega t & 0 \\ \sin 2\omega t & 1 - \cos 2\omega t & 0 \\ 0 & 0 & 0 \end{pmatrix}, \quad (2.3)$$

where $\omega = \sqrt{\frac{2GM}{R^3}}$ is the frequency. The power then scales as

$$\mathcal{P} \sim G \ddot{Q}^2 \sim \frac{G^4 M^5}{R^5}. \quad (2.4)$$

For a system of two objects with masses $M \gg m$, the power scales as

$$\mathcal{P} \sim \frac{G^4 M^3 m^2}{R^5}. \quad (2.5)$$

Let us compute this for the Earth-Sun system. To do that, we need to reintroduce factors of c . Through dimensional analysis, one writes

$$\mathcal{P} \sim \frac{G^4 M^3 m^2}{R^5 c^5}. \quad (2.6)$$

The Earth has a mass $m = 5.97 \times 10^{24} \text{ kg}$, and orbits at about $R = 1.5 \times 10^8 \text{ km}$ from the Sun, which has a mass $M = 1.989 \times 10^{30} \text{ kg}$. Hence, the power emitted by the gravitational radiation of the Earth-Sun system is $\approx 30 \text{ W}$, which is a negligible amount. Just to have an idea, the power output of the Sun is $3.8 \times 10^{26} \text{ W}$. Thus, the only gravitational waves we can detect originate in extreme scenarios, such as collisions of highly compact objects. Despite that, since gravitational waves get damped as they propagate, when they reach us on Earth, they have small amplitudes. The amplitude of a GW, h , is a measure of the ratio by which spacetime is stretched or compressed. It is related to the variation of the

mass properties of the emitting body by the quadrupole formula

$$h = \frac{2G}{c^4} \frac{1}{R} \frac{\partial^2 Q}{\partial t^2}, \quad (2.7)$$

where R is the distance from the source to the detector, and Q is the quadrupole moment of the source. The first detected GW, for instance, had an amplitude $h \sim 10^{-22}$. This difficulty made them undetectable to us for about 100 years after their prediction. To detect them, interferometers have been built with arms that extend for kilometers. GWs were first detected by the LIGO in 2015 [1,2], and their study can provide new key insights into the physics of the universe.

In this chapter, we will discuss where this all comes from. We start by explaining the ideas that led to the postulation of GR and introduce important geometric concepts. Finally, we explore how GWs emerge in GR.

2.1 Brief Review of General Relativity

2.1.1 Introduction

Postulated by Einstein more than 100 years ago [4], GR is the most accurate theory of gravity to date. It has been extensively tested (see for instance [5]), and all the predictions tested so far turned out to be correct. GR revolutionized the way we think of gravity, by explaining it as a manifestation of the curvature of spacetime, instead of as a force acting at a distance. In the words of John A. Wheeler, "matter tells spacetime how to curve, and spacetime tells matter how to move" [6].

When developing this theory, Einstein was inspired by three principles:

- **The principle of general covariance**, which states that the form of physical laws is invariant under any arbitrary differentiable coordinate transformation.
- **The principle of equivalence**, which states that all test objects fall with the same trajectory in a gravitational field regardless of their mass.
- **Mach's principle**, which says that the local inertial properties of objects are determined by the quantity and distribution of matter in the universe.

2.1.2 Curved spacetime

In General Relativity, the metric tensor, $g_{\mu\nu}$, is the fundamental object of study. It determines causality, by defining the speed of light, faster than which no signal can travel. The metric is a symmetric (0,2) tensor, usually defined to be nondegenerate – which allows us to define the inverse metric $g^{\mu\nu}$.

In a curved space, we need to define a generalization of the partial derivative, the covariant derivative ∇_μ , which is a way of specifying a derivative along tangent vectors of a manifold. To define it, one introduces a unique object relating vectors in tangent spaces of nearby points that we can construct from the metric, the Christoffel symbols. For the commonly chosen case of metric compatibility, where the covariant derivative of the metric with respect to the Christoffels vanishes everywhere, i.e. $\nabla_\alpha g_{\mu\nu} = 0$, they take the form

$$\Gamma^\lambda_{\mu\nu} = \frac{1}{2}g^{\lambda\sigma}(\partial_\mu g_{\nu\sigma} + \partial_\nu g_{\mu\sigma} - \partial_\sigma g_{\mu\nu}). \quad (2.8)$$

The information about the curvature of a manifold is encrypted in the Riemann tensor

$$R^\rho_{\sigma\mu\nu} = \partial_\mu \Gamma^\rho_{\nu\sigma} - \partial_\nu \Gamma^\rho_{\mu\sigma} + \Gamma^\rho_{\mu\lambda} \Gamma^\lambda_{\nu\sigma} - \Gamma^\rho_{\nu\lambda} \Gamma^\lambda_{\mu\sigma}. \quad (2.9)$$

The curvature of spacetime dictates the motion of the bodies within it. The EFE are a set of 10 non-linear partial differential equations that relate certain components of the Riemann tensor with the energy-momentum tensor $T_{\mu\nu}$,

$$R_{\mu\nu} - \frac{1}{2}g_{\mu\nu}R = 8\pi T_{\mu\nu}, \quad (2.10)$$

where $R_{\mu\nu} = R^\lambda_{\mu\lambda\nu}$ is the Ricci tensor, and $R = R^\mu_{\mu}$ is the Ricci scalar. The EFE incorporate the relation between the geometry of spacetime and the distribution of mass and energy.

2.2 Linearized Theory

To study the emergence of GWs in GR, one follows the approach of Linearized Theory, which consists of expanding the Einstein field equations around a known solution.

2.2.1 Expansion around flat space

Consider the metric perturbed around flat spacetime

$$g_{\mu\nu} = \eta_{\mu\nu} + \epsilon h_{\mu\nu}, \quad (2.11)$$

where $|\epsilon| \ll 1$. The linearized Riemann tensor, $\tilde{R}^\rho_{\sigma\mu\nu}$, is given by

$$\tilde{R}^\rho_{\sigma\mu\nu} = \lim_{\epsilon \rightarrow 0} \partial_\epsilon R^\rho_{\sigma\mu\nu}, \quad (2.12)$$

i.e. we can compute the linearized Riemann tensor by substituting the expression for the metric (2.11) in the definition (2.9) and keeping only the linear terms in $h_{\mu\nu}$.

Let us then obtain the linearized version of the EFE. We start by noting that, since we are working up to linear order, indices are raised and lowered with the Minkowski metric $\eta_{\mu\nu}$. The inverse metric to leading order reads

$$g^{\mu\nu} = \eta^{\mu\nu} - \epsilon h^{\mu\nu}. \quad (2.13)$$

Since the Christoffel symbols are expressed in terms of derivatives of the perturbation $h_{\mu\nu}$, we can discard the terms $\Gamma\Gamma$ of the Riemann tensor because they are of second-order in h . Thus, the Riemann tensor to linear order is given by

$$R^\sigma{}_{\rho\mu\nu} = \partial_\mu \Gamma^\sigma{}_{\nu\rho} - \partial_\nu \Gamma^\sigma{}_{\mu\rho} \quad (2.14)$$

$$= \frac{1}{2} \eta^{\sigma\lambda} (\partial_\mu \partial_\rho h_{\nu\lambda} - \partial_\mu \partial_\lambda h_{\nu\rho} - \partial_\nu \partial_\rho h_{\mu\lambda} + \partial_\nu \partial_\lambda h_{\mu\rho}). \quad (2.15)$$

The Ricci tensor is then given by

$$R_{\mu\nu} = \frac{1}{2} (\partial^\rho \partial_\mu h_{\nu\rho} + \partial^\rho \partial_\nu h_{\mu\rho} - \square h_{\mu\nu} - \partial_\mu \partial_\nu h), \quad (2.16)$$

where $h = h^\mu{}_\mu$ is the trace of $h_{\mu\nu}$ and $\square = \partial^\mu \partial_\mu$, and the Ricci scalar by

$$R = \partial^\mu \partial^\nu h_{\mu\nu} - \square h. \quad (2.17)$$

As one can already guess from Eqs. (2.16) and (2.17), the EFE look rather cumbersome. They can however be written more compactly by defining

$$\bar{h}_{\mu\nu} = h_{\mu\nu} - \frac{1}{2} \eta_{\mu\nu} h. \quad (2.18)$$

Finally, the linearized Einstein equations yield

$$\square \bar{h}_{\mu\nu} + \eta_{\mu\nu} \partial^\rho \partial^\sigma \bar{h}_{\rho\sigma} - \partial^\rho \partial_\nu \bar{h}_{\mu\rho} - \partial^\rho \partial_\mu \bar{h}_{\nu\rho} = -16\pi T_{\mu\nu}, \quad (2.19)$$

with $c = G = 1$, and $T_{\mu\nu}$ the energy-momentum tensor.

2.2.2 Gauge freedom

According to the principle of general covariance, the laws of physics must take the same form for all observers. This means that physical quantities must not depend on the frame of reference, or coordinate system – in other words, physical quantities are invariant under any coordinate transformation

$$x^\mu \rightarrow x'^\mu(x), \quad (2.20)$$

where x'^μ is a smooth function of x^μ .

If we impose Eq. (2.11), we have that, under the infinitesimal local transformation

$$x^\mu \rightarrow x'^\mu = x^\mu + \epsilon \xi^\mu(x), \quad (2.21)$$

where $|\epsilon| \ll 1$, the metric transforms like

$$g_{\mu\nu}(x) \rightarrow g'_{\mu\nu}(x') = \frac{\partial x^\rho}{\partial x'^\mu} \frac{\partial x^\sigma}{\partial x'^\nu} g_{\rho\sigma}(x). \quad (2.22)$$

Thus, plugging in the expression for the perturbed metric (2.11), and taking the first-order terms yields

$$h_{\mu\nu}(x) \rightarrow h'_{\mu\nu}(x') = h_{\mu\nu}(x) - 2\partial_{(\mu}\xi_{\nu)}. \quad (2.23)$$

The perturbed metric reads

$$g'_{\mu\nu} = \eta_{\mu\nu} + \epsilon (h_{\mu\nu}(x) - 2\partial_{(\mu}\xi_{\nu)}). \quad (2.24)$$

The infinitesimal coordinate transformation (2.21) does not spoil the condition that the term added to the Minkowski metric must be $\mathcal{O}(\epsilon)$. Consequently, these infinitesimal local transformations are a symmetry of the linearized theory. Under the coordinate transformation (2.21), \bar{h} transforms as

$$\bar{h}_{\mu\nu}(x) \rightarrow \bar{h}'_{\mu\nu}(x') = \bar{h}_{\mu\nu}(x) - 2\partial_{(\mu}\xi_{\nu)} + \eta_{\mu\nu}\partial_\alpha\xi^\alpha. \quad (2.25)$$

Consequently, we have

$$\partial^\nu \bar{h}_{\mu\nu}(x) \rightarrow \partial^\nu \bar{h}'_{\mu\nu}(x') = \partial^\nu \bar{h}_{\mu\nu}(x) - \partial^\nu \partial_\nu \xi_\mu. \quad (2.26)$$

We can choose ξ_μ such that

$$\partial^\nu \bar{h}_{\mu\nu}(x) - \partial^\nu \partial_\nu \xi_\mu = 0. \quad (2.27)$$

This is just the wave equation for ξ_μ with a source term $\partial^\nu \bar{h}_{\mu\nu}$. Therefore, we can always choose a gauge such that

$$\partial^\nu \bar{h}_{\mu\nu} = 0. \quad (2.28)$$

This is known as the harmonic gauge (or Lorentz gauge). In this gauge, the linearized Einstein equations (2.19) reduce to an inhomogeneous wave equation

$$\square \bar{h}_{\mu\nu} = -16\pi T_{\mu\nu}, \quad (2.29)$$

where we are considering the system of natural units $G = c = 1$.

2.2.3 The Transverse-Traceless gauge

Consider the vacuum solution of the linearized Einstein equations,

$$\square \bar{h}_{\mu\nu} = 0. \quad (2.30)$$

A solution to this equation is given by

$$\bar{h}_{\mu\nu} = \text{Re}(H_{\mu\nu} e^{ik_\alpha x^\alpha}), \quad (2.31)$$

where $H_{\mu\nu}$ is a complex, symmetric polarization matrix, and k^μ is the wave vector. The expression in Eq. (2.31) will solve the wave equation (2.30) if the wave vector is null, i.e. $k_\alpha k^\alpha = 0$. Thus, gravitational waves, like electromagnetic waves, travel at the speed of light.

Since $H_{\mu\nu}$ is a 4×4 symmetric matrix, it has 10 independent components. However, it is important to note that the linearized equations only take the form (2.30) in harmonic gauge, which implies

$$k^\mu H_{\mu\nu} = 0. \quad (2.32)$$

This tells us that the polarization is orthogonal to the direction of propagation, and imposes four conditions on the polarization matrix, leaving it with six independent components. However, the condition (2.32) does not fix the gauge completely.

We can add to ξ^μ a vector $\tilde{\xi}^\mu$ such that $\square \tilde{\xi}^\mu = 0$, therefore respecting the harmonic gauge condition. In particular, we can take

$$\tilde{\xi}^\mu = \lambda^\mu e^{ik_\alpha x^\alpha}. \quad (2.33)$$

Under this transformation, the polarization matrix changes as

$$H_{\mu\nu} \rightarrow H'_{\mu\nu} = H_{\mu\nu} + i(2k_{(\mu} \lambda_{\nu)} - k^\alpha \lambda_\alpha \eta_{\mu\nu}). \quad (2.34)$$

Thus, there are four extra degrees of freedom λ_μ that reduce the total independent components of $H_{\mu\nu}$ to two. In particular, we can choose

$$H_{0\mu} = 0, \quad H^\mu{}_\mu = 0. \quad (2.35)$$

This is known as the Transverse-Traceless (TT) gauge.

There is a common conceptual confusion in the literature, which fails to distinguish this notion of TT

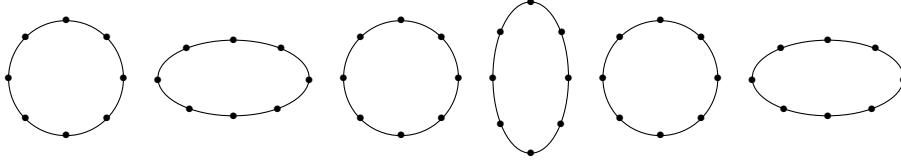


Figure 2.1: Representation of how a set of pointlike particles initially distributed in a circle are perturbed by a GW traveling perpendicularly to them when $H_{\times} = 0$.

gauge from the relevant modes extracted using a projection operator when studying the GWs emitted by an isolated system. Whereas TT gauge is local in momentum space, the latter is local in physical space, and it has been shown that this difference persists even in the asymptotic region [7, 8]. In this work, we shall refer to the concept introduced in Eq. (2.35) as TT gauge (or differential TT gauge), and the other as transverse-traceless (tt) gauge (or projection tt gauge).

2.2.3.A Physical intuition of the propagating degrees of freedom

Consider a wave propagating in the z direction with frequency ω . The wavevector is given by

$$k_{\mu} = (\omega, 0, 0, \omega). \quad (2.36)$$

From Eqs. (2.32) and (2.35), one concludes that the polarization matrix must have the form

$$H_{\mu\nu} = \begin{pmatrix} 0 & 0 & 0 & 0 \\ 0 & H_{+} & H_{\times} & 0 \\ 0 & H_{\times} & -H_{+} & 0 \\ 0 & 0 & 0 & 0 \end{pmatrix}. \quad (2.37)$$

H_{+} and H_{\times} are the two polarization states. A brief description of the intuition behind these quantities is given.

The geodesic deviation equation – which relates the curvature with the deviation of the geodesics of two freefall test particles relative to each other – in the linearized theory reduces to

$$\frac{d^2 S^{\mu}}{dt^2} = \frac{1}{2} \frac{d^2 h^{\mu}_{\nu}}{dt^2} S^{\nu}, \quad (2.38)$$

where S^{μ} is the displacement vector. Consider a collection of pointlike particles arranged in a circle at time $t = 0$. This corresponds to the initial configuration $S^1(0)^2 + S^2(0)^2 = R^2$, where R is the radius of the circle. If we set H_{\times} to zero, the solution for S^{μ} is up to linear order in h given by

$$S^1(t) \approx S^1(0) \left(1 + \frac{1}{2} H_{+} e^{i\omega t}\right), \quad S^2(t) \approx S^2(0) \left(1 - \frac{1}{2} H_{+} e^{i\omega t}\right). \quad (2.39)$$

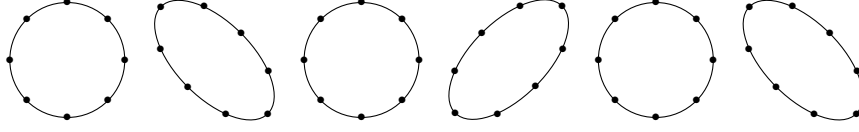


Figure 2.2: Representation of how a set of pointlike particles initially distributed in a circle are perturbed by a GW traveling perpendicularly to them when $H_+ = 0$.

This solution corresponds to the configuration shown in Fig. 2.1, where the geometric forms represent how spacetime is perturbed by a GW traveling perpendicularly to them.

On the other hand, if we set $H_+ = 0$, the solution to the geodesic deviation equation will be

$$S^1(t) \approx S^1(0) + \frac{1}{2}S^2(0)H_{\times}e^{i\omega t}, \quad S^2(t) \approx S^2(0) + \frac{1}{2}S^1(0)H_{\times}e^{i\omega t}, \quad (2.40)$$

which corresponds to the displacement of geodesics in Fig. 2.2.

3

Approaches to the weak-field regime in Numerical Relativity

Contents

3.1	Wave extraction, Cauchy-Characteristic matching, and extraction	16
3.2	Hyperboloidal compactification	18
3.3	Conformal formalism	19
3.4	The good-bad-ugly model	21

Gravitational waves, like electromagnetic (EM) waves, carry information about the source(s) that originated them. Until the detection of GWs in 2017, physicists relied on EM waves to study the universe. However, with the possibility of detecting GWs, we have access to more information which will help us to understand our universe better. For instance, we can study systems like colliding black holes that have no EM counterpart. Furthermore, GWs interact very weakly with matter, contrary to EM radiation, which gets altered easily.

To detect gravitational radiation, theoretical waveforms are compared with data gathered by the GW detectors to look for matching signals and, upon detection, get information about the systems that originated that radiation. Thus, waveforms are the main deliverable of numerical relativity for gravitational wave astronomy. The form of signals emitted by a given gravitational radiation source is impossible to obtain analytically since there is no underlying symmetry that can simplify the EFE. Therefore, numerical methods have been developed to obtain these waveforms. In this chapter, we present the state-of-the-art methods used, and a new approach using hyperboloidal compactification.

In the EFE, space and time are treated equally. Although it has been an important learning from GR, there are situations where we are interested in the dynamical evolution of gravity in time. In practice, this requires breaking the coordinate invariance – albeit the solutions will still be covariant – i.e. treating time differently, and slicing the spacetime to obtain an appropriate hypersurface where initial data can be specified.

3.1 Wave extraction, Cauchy-Characteristic matching, and extraction

The most common way to extract a GW signal at future null infinity is by computing the relevant quantities at several radii and performing an extrapolation to future null infinity (see, for instance, [9–11]). A stricter approach would be to compute these quantities directly at \mathcal{I}^+ . To do this, we can foliate the spacetime into hypersurfaces that reach future null infinity. There are two important ways of foliating the spacetime into hypersurfaces where the initial data is specified, known as Cauchy and characteristic slices.

Cauchy slices are constant-time spacelike hypersurfaces that extend from the origin to spatial infinity (i_0). Since one cannot have an infinite computational grid, Cauchy slices have the drawback of having to be cut at a given value of the radial coordinate and only the interior domain can be evolved. The artificial boundary that is created has the disadvantage that the slices no longer reach infinity, where the gravitational radiation is unambiguously defined, and one has to introduce boundary conditions that are difficult to state.

Characteristic slices, on the other hand, are outgoing null hypersurfaces that represent the paths followed by light rays (or any radiation that travels at the speed of light) and reach \mathcal{I}^+ . This type of

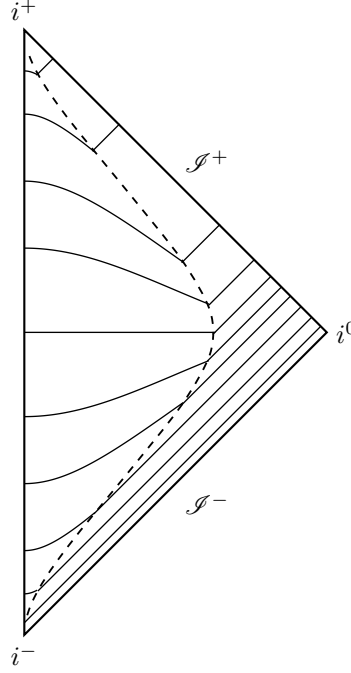


Figure 3.1: Penrose diagram of Minkowski spacetime foliated along Cauchy and characteristic slices.

foliation is suitable for GW radiation extraction since they reach future null-infinity (\mathcal{I}^+). Nonetheless, null coordinates are not appropriate to evolve a strong-field region, since coordinate singularities arise in these scenarios.

The complementarity of the advantages and disadvantages of these foliations (the first is appropriate to describe the strong-field region, whereas the second is suitable to evolve the weak-field region) suggested their combination. Two important methods arose from this conclusion, Cauchy-Characteristic matching (CCM) and CCE, where the spacetime is foliated into both Cauchy and characteristic slices (see, for instance, [12]). This combination is illustrated for Minkowski in Fig. 3.1. The dashed line represents a time-like hypersurface that separates the two domains. The interior region, at the left of the boundary, is foliated into Cauchy slices, and the exterior region, at the right, into characteristic slices.

In CCM the strong-field region is described by Cauchy evolution, and the weak-field region is described by characteristic evolution. These evolutions are matched at the time-like interface. The data from the Cauchy evolution serves as initial data for the characteristic evolution, and the characteristic data is used in the boundary conditions for the Cauchy evolution. Unfortunately, this method has not been implemented successfully due to the stability problems that arise when communicating data at the interface between the Cauchy and characteristic domains.

CCE is the current optimal method to numerically obtain the waveform signal of a given source of gravitational radiation. In this approach, the characteristic evolution uses data from the Cauchy evolution for the inner boundary conditions, but it does not provide data for the boundary conditions of the Cauchy

evolution. Thus, instead of solving the Initial Value Problem (IVP), we solve an Initial Boundary Value Problem (IBVP). In this way, one manages to work around the instabilities that arise in CCM. However, even at the continuum level for a well-posed IBVP on the Cauchy domain, the unphysical boundary necessarily causes reflections, which are not present in the IVP. This is therefore a systematic modeling error and as such cannot converge with resolution to the true solution of the IVP. This is unsatisfactory from a first-principles viewpoint since evolving for an extended period of time yields worse results. Besides that, the equations that are solved in CCE are not well-posed in the relevant norms as shown in [13, 14]. It is in this setting that the work of this thesis arises – computing gravitational waves all the way out to future null infinity from first principles.

3.2 Hyperboloidal compactification

Another approach used to extract gravitational waves at future null infinity is to foliate spacetime into hyperboloidal slices. To do that, we need to perform a hyperboloidal compactification, i.e. introduce hyperboloidal coordinates that bring \mathcal{I}^+ to a finite coordinate distance. This is done in two steps: the first consists of selecting a time parameter whose level sets are hyperboloidal slices (hyperboloidal time), and the second brings in the compactification of the radial coordinate on those slices. A detailed discussion of this process can be found in [15].

Let us consider the example of the hyperboloidal compactification of Minkowski spacetime and its use with the wave equation. We can bring spatial infinity to a finite coordinate distance by performing a compactification in the outgoing direction, R in spherical coordinates. We introduce a compactifying coordinate r such that $R = \frac{r}{\Omega(r)}$ and require that the gradient of $\Omega(r)$, known as the conformal factor, does not vanish when $\Omega(r) = 0$, which corresponds to infinity in R . We could also do this for a Cauchy slice, but the loss of resolution of signals propagating near spatial infinity creates numerical problems and, besides, we are not getting to \mathcal{I}^+ . With that in mind, we also need to introduce a new time coordinate, t , to ensure that the slices reach future null infinity (\mathcal{I}^+) – not just spatial infinity (i_0) – and to avoid loss of resolution. We, therefore, define t as

$$t = T - H(r), \quad (3.1)$$

where $H(r)$, known as the height function, must satisfy $|dH/dR| < 1$ so that t is a time function and $\lim_{R \rightarrow \infty} dH/dR = 1$ so that it becomes retarded time near infinity.

Consider the case of 1+1 dimensions. The wave equation reads

$$(-\partial_T^2 + \partial_R^2)\psi = 0. \quad (3.2)$$

In compactified hyperboloidal coordinates, this turns into

$$\left[\partial_t^2 + \frac{\Omega^2}{(1-h^2)L} (2h\partial_t\partial_r - \frac{\Omega^2}{L}\partial_r^2 + \partial_r h\partial_t - \partial_r \frac{\Omega^2}{L}\partial_r) \right] \psi = 0, \quad (3.3)$$

where $h \equiv \frac{dH}{dR}(r)$ and $L \equiv \Omega - r \frac{d\Omega}{dr}$. We choose $H(R) = \sqrt{S^2 + R^2}$ and set the compress function to

$$\Omega = \frac{1}{2} \left(1 - \frac{r^2}{S^2} \right). \quad (3.4)$$

Thus, $S = \pm r$ is the coordinate location of null infinity, where the wave equations become

$$\partial_t(\partial_t \pm 2\partial_r)\psi = 0, \quad (3.5)$$

which indicates that both boundaries are outflow, and boundary conditions are not needed.

In multiple spatial dimensions, the regularization of the equations at future null infinity is not as straightforward. In 3+1 dimensions, the scalar wave equation in spherical coordinates (T, R, θ, ϕ) is

$$\left(-\partial_T^2 + \partial_R^2 + \frac{2}{R}\partial_R + \frac{1}{R^2}\Delta_{\mathbb{S}^2} \right) \psi = 0, \quad (3.6)$$

where $\Delta_{\mathbb{S}^2}$ is the Laplace operator on the 2-sphere. The angular term admits a regular compactification since, under compactification, it is multiplied by Ω^2 , whereas the first radial derivative term leads to a singular operator at infinity. This problem can be solved by rescaling the field such that it attains a non-vanishing finite limit at future null infinity. In three spatial dimensions, fields that satisfy the wave equation decay as R^{-2} . We define the rescaled field $\Psi = R\psi$. The wave equation for this new variable is

$$\left(-\partial_T^2 + \partial_R^2 + \frac{1}{R^2}\Delta_{\mathbb{S}^2} \right) \Psi = 0, \quad (3.7)$$

which is regular under compactification. In Sec. 3.4, we discuss a model of GR that allows us to understand how to rescale the fields that describe GWs.

By performing this hyperboloidal compactification, we foliate spacetime into hypersurfaces that are spacelike everywhere and extend from the origin to future null infinity. They are called hyperboloidal slices and are represented in Fig. 3.2 for Minkowski spacetime.

3.3 Conformal formalism

In this section, we present an alternative approach to CCM that uses hyperboloidal slices, where initial data can be specified. The idea of this approach is to “bring infinity closer”. Though the physical distance is infinite, we can always introduce a set of coordinates that brings infinity to a finite coordinate distance.

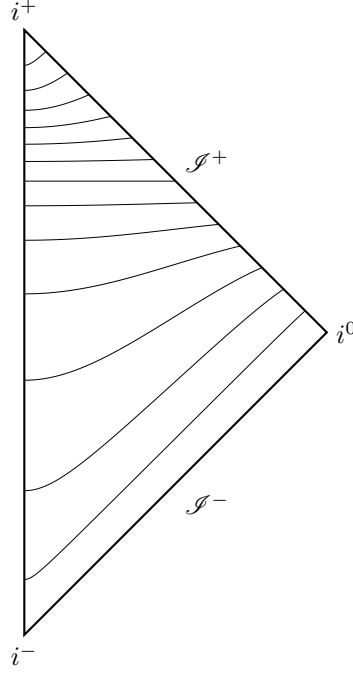


Figure 3.2: Penrose diagram of Minkowski spacetime foliated along hyperboloidal slices.

However, this compactification implies that the metric becomes infinite. This is solved by evolving a conformal (unphysical) metric $\tilde{g}_{\mu\nu}$ related to the physical metric of spacetime $\bar{g}_{\mu\nu}$

$$\tilde{g}_{\mu\nu} = \Omega^{-2} \bar{g}_{\mu\nu}, \quad (3.8)$$

where Ω is called the conformal factor and is defined such that it vanishes when the metric is infinite, thus giving a conformal metric that is finite everywhere. This idea was introduced by Penrose [16]. In this approach, we can unambiguously extract gravitational radiation (as well as other quantities that can only be consistently defined at infinity). However, by simply substituting Eq. (3.8) in the EFE we get a singular expression for $\Omega = 0$. This issue was solved by Friedrich [17], which introduced conformal field equations that are regular equations for $\bar{g}_{\mu\nu}$ and certain additional independent variables.

However, this approach also poses some problems, such as the construction of hyperboloidal initial data, the choice of a good gauge, and the stability of the evolutions against constraint violation.

Alternatively, we can also evolve the full four-dimensional spacetime metric as was done in the pioneering works of Hahn and Lindquist in 1964 [18] – the first documented effort to generate black hole spacetimes by numerically solving the EFE – and Pretorius in 2005 [19] – one of the first simulation of black hole binaries through inspiral, merger and ringdown.

3.4 The good-bad-ugly model

The good-bad-ugly (GBU) model is a model of GR. It represents the three types of field equations that are included in the EFE, and consists of the following equations

$$\square g \simeq 0, \quad (3.9a)$$

$$\square b \simeq (\nabla_T g)^2, \quad (3.9b)$$

$$\square u \simeq \frac{2}{R} \nabla_T u, \quad (3.9c)$$

where g stands for *good*, b for *bad*, and u for *ugly*. In this work, we will not be interested in *bad* fields, since we are focusing on the linearized theory where non-linear equations like (3.9b) do not appear.

Good fields decay like a solution to the wave equation, whereas *ugly* fields decay faster near future null infinity. A careful discussion of the asymptotics of these fields can be found in [20]. By modeling the linearized EFE as *good* and *ugly* equations, we can understand the rate of decay of the fields, which will in turn help us understand how to rescale them such that they attain a non-vanishing finite limit at future null infinity. The propagating degrees of freedom manifest in the curvature, h_+ and h_\times , will be modeled as *goods* since they are the quantities we measure on Earth (i.e. they should not decay as fast as all the other quantities), whereas the other eight independent metric components will be modeled as *uglies*. We will return to this topic in chapter 5.

4

Numerical methods

Contents

4.1	Finite differences	24
4.2	Method of Lines	25
4.3	Convergence testing	26

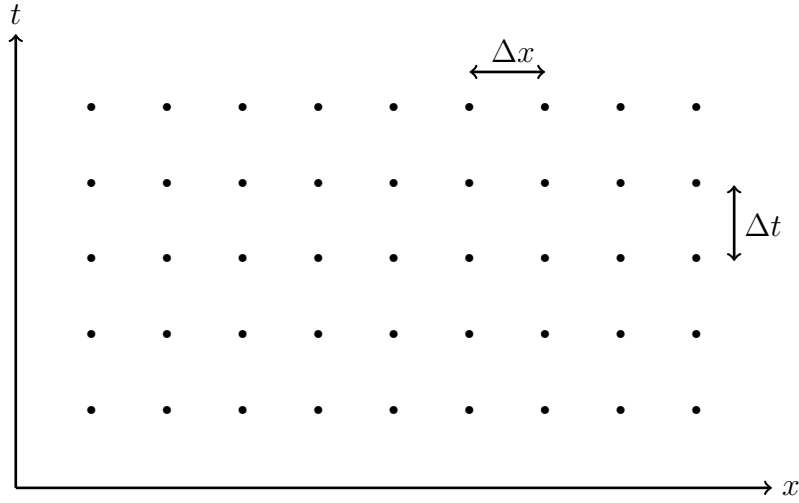


Figure 4.1: Representation of the computational grid.

As we saw in Chapter 2, the EFE are a set of ten non-linear, coupled partial differential equations (PDEs). These features make them extremely hard to solve analytically. One can only do so in very special scenarios, either when there is an underlying symmetry that significantly simplifies the problem or by making assumptions. To study more complex phenomena, like the inspiral and merger of compact objects, we resort to numerical methods. These allow us to obtain accurate approximate solutions to complex problems that would otherwise be unsolvable. In this chapter, we introduce the theoretical reasoning behind the numerical approach taken in this work. A more in-depth explanation of the numerical methods used to solve problems in GR can be found in [21–23].

4.1 Finite differences

The most popular methods to solve partial differential equations numerically are finite differencing, finite elements, and spectral methods. We shall focus on the first since it was the one used in the present work.

Computers have only finite memory, hence, when trying to solve a PDE numerically, we must find a way to discretize the field we are solving for. In the finite differencing method, this is done by first discretizing the spacetime itself. Then, instead of a continuum, the spacetime is described by a set of discrete points – called the computational grid – illustrated in Fig. 4.1 for a 1+1 dimensional spacetime. The distances in space do not necessarily have to be uniform, but we will consider it so, given that in this work we only worked with computational grids with uniform spacing between points, Δx . Δt denotes the time step.

The next step is the discretization of the differential equations themselves. This is done by approxi-

imating the differential operators by finite differences between values of the involved functions at nearby points. Instead of one differential equation, we are then left with several coupled algebraic equations.

Consider, for instance, a field $u(t, x)$. Discretizing the domain of u would mean having points at

$$x_i = x_0 + i\Delta x, i = 0, \dots, I \quad (4.1a)$$

$$t_n = t_0 + n\Delta t, n = 0, \dots, N \quad (4.1b)$$

$$u_i^n = u(t_n, x_i) \quad (4.1c)$$

In this example, a first spatial derivative would be approximated to order $\mathcal{O}(n^2)$ by the finite difference

$$\frac{\partial u}{\partial x} = \frac{u_{i+1}^n - u_{i-1}^n}{2\Delta x} + \mathcal{O}(\Delta x) \approx \frac{u_{i+1}^n - u_{i-1}^n}{2\Delta x}. \quad (4.2)$$

This approximation has an associated error that is called truncation error, τ_Δ . It is defined as the result of acting with a finite difference operator in the solution to the original differential equation, and it scales with a power of the grid spacing Δ . The scaling power determines the order of the approximation. We say that a consistent approximation is of order n if

$$\lim_{\Delta \rightarrow 0} \tau_\Delta \sim \Delta^n. \quad (4.3)$$

There is yet another error associated with the finite differencing approximation, called the solution error ϵ_Δ . It is defined as

$$\epsilon_\Delta \equiv u - u_\Delta, \quad (4.4)$$

where u is the exact solution to the original differential equation, and u_Δ is the exact solution to the finite difference equation. This error defines the concept of convergence. We say a finite difference approximation converges if ϵ_Δ goes to zero in the continuum limit. We will address how to test convergence in section 4.3.

4.2 Method of Lines

The Method of Lines (MOL) is an approach to solving evolution equations, in which the discretization of space and time are made separately. Consider, for instance, a scalar PDE of the form

$$\partial_t u = D(u), \quad (4.5)$$

where D is an arbitrary spatial differential operator. By discretizing only the spatial derivatives, equation (4.5) can be rewritten as a coupled system of Ordinary Differential Equations (ODEs). Consider, for

example, the advection equation in 1+1 dimensions

$$\partial_t u = -\partial_x u. \quad (4.6)$$

By discretizing the spatial derivative like in Eq. (4.2), we then arrive at the system of ordinary differential equations

$$\frac{du_i}{dt} = -\frac{u_{i+1} - u_{i-1}}{2\Delta x}, \quad (4.7)$$

Given these equations, we can now use any ODE discretization technique to find approximate solutions, e.g. the Euler method or higher-order methods such as Runge-Kutta methods.

In particular, a common method to integrate in time is the fourth-order Runge-Kutta (RK4). Using RK4, each time step is calculated via

$$u^{n+1} = u^n + \frac{\Delta t}{6}(k_1 + 2k_2 + 2k_3 + k_4), \quad (4.8)$$

where k_1 , k_2 , k_3 and k_4 are recursively computed in the following way

$$k_1 = D(u^n), \quad (4.9a)$$

$$k_2 = D(u^n + k_1 \Delta t/2), \quad (4.9b)$$

$$k_3 = D(u^n + k_2 \Delta t/2), \quad (4.9c)$$

$$k_4 = D(u^n + k_3 \Delta t). \quad (4.9d)$$

This method is commonly referred to as MOL-RK4.

4.3 Convergence testing

Numerical methods are very useful to calculate solutions to a given equation that would otherwise be impossible to solve analytically. Nonetheless, by performing a numerical calculation at only one resolution – in the case of the aforementioned example, this means calculating the solution at only one value of Δx and Δt – one cannot know if the result obtained is close to the correct solution.

The numerical solution obtained is said to converge if it gets closer to the exact solution at the appropriate rate as resolution is increased. There are two important notions of convergence that we use in this work, pointwise and norm convergence. While norm convergence is typically used in numerical analysis and can, at least for certain model problems, be proved mathematically, pointwise convergence is a useful tool in computational physics that allows us to understand what is happening locally, e.g.

understanding if an error is coming from the origin or the boundary conditions.

The solution to a stable finite difference approximation of order n can be interpreted as a continuum function that can be expanded as a power series of the discretization parameter Δ

$$u_{\Delta} \sim u + \epsilon(\Delta)^n, \quad (4.10)$$

where u is the solution of the original PDE. Thus, if we increase the resolution by p , i.e. Δ/p , we should also have that

$$u_{\Delta/p} \sim u + \epsilon\left(\frac{\Delta}{p}\right)^n, \quad (4.11a)$$

$$u_{\Delta/p^2} \sim u + \epsilon\left(\frac{\Delta}{p^2}\right)^n. \quad (4.11b)$$

Using Eqs. (4.10), (4.11a), and (4.11b), one can deduce that in the limit $\Delta \rightarrow 0$

$$\frac{u_{\Delta} - u_{\Delta/p}}{u_{\Delta/p} - u_{\Delta/p^2}} = p^n. \quad (4.12)$$

In order to test pointwise convergence, one plots the grid functions $u_{\Delta} - u_{\Delta/p}$ and $p^n(u_{\Delta/p} - u_{\Delta/p^2})$, where the differences can be taken by interpolating onto the same grid or calculated at shared grid points. If these “line up”, i.e. if their difference at each point is less than a small value, then we say the code converges pointwise everywhere. If there is a point where the difference between the two functions is large, we say the code does not converge at that point.

We define the norm convergence factor by taking the norm of the denominator and numerator in Eq. (4.12)

$$c(t) \equiv \frac{\|u_{\Delta} - u_{\Delta/p}\|}{\|u_{\Delta/p} - u_{\Delta/p^2}\|}. \quad (4.13)$$

Usually, the L2-norm is used, although other options are possible. By taking the norm at a given time, we are integrating in space and therefore get a function that only depends on time. In the continuum limit, we obtain the same limit as (4.12).

In any numerical calculation, one should test if the numerical solutions converge, i.e. if the convergence factor (4.13) behaves as expected. By testing the code's convergence, one can also estimate the solution errors associated with the results. We will see applications of these ideas in chapter 6.

5

Gravitational Waves in Hyperboloidal Slices

Contents

5.1 Geometric Setup	30
5.2 Regularization at the origin	32
5.3 Regularization at future null infinity	35
5.4 Model equations	38

In this chapter, we derive the field equations for linearized GR on hyperboloidal slices. We start by introducing the geometrical setup, where we express the ten independent metric components as a set of physical variables and linearize them. We then study the regularization of both the origin and future null infinity. The appropriate rate of decay of the fields is imposed in two ways: first, we fix the gauge, and second, we make constraint additions to the equations. The equations obtained are modeled by two *goods* and eight *uglies*, as introduced in Section 3.4.

5.1 Geometric Setup

5.1.1 Geometric quantities

We define the outgoing and incoming null vectors, respectively, as

$$\xi^\mu = \partial_T^\mu + C_+^R \partial_R^\mu, \quad (5.1)$$

$$\underline{\xi}^\mu = \partial_T^\mu + C_-^R \partial_R^\mu, \quad (5.2)$$

where the quantities C_\pm^R can be interpreted as coordinate light speeds. Derivatives along the outgoing null direction ξ^μ and angular derivatives are called good derivatives since they improve the fall-off of the fields they are applied to. On the other hand, derivatives along the ingoing null direction $\underline{\xi}^\mu$ are called bad derivatives since they do not change the rate of decay of the fields.

The co-vectors are defined as

$$\eta_\mu = -C_+^R \nabla_\mu T + \nabla_\mu R - C_A^+ \nabla_\mu \theta^A, \quad (5.3)$$

$$\underline{\eta}_\mu = C_-^R \nabla_\mu T - \nabla_\mu R + C_A^- \nabla_\mu \theta^A, \quad (5.4)$$

where $A = \theta, \phi$.

The inverse metric can be expressed as

$$g^{\mu\nu} = -\frac{2e^{-\varphi}}{\tau} \xi^{(\mu} \underline{\xi}^{\nu)} + g^{\mu\nu}, \quad (5.5)$$

where $\tau = C_+^R - C_-^R$. The first term of Eq. (5.5) encapsulates the radial causal structure of spacetime, and φ is related to its determinant. The last term, $g^{\mu\nu}$, captures the physics along the directions orthogonal to the radial null directions. It is the inverse of a 4×4 symmetric matrix whose only non-vanishing components are the angular ones

$$g_{\mu\nu} = \mathring{R}^2 q_{\mu\nu}, \quad (5.6)$$

where we define the 2-metric $q_{\mu\nu}$ as

$$q_{\mu\nu} = \begin{pmatrix} 0 & 0 & 0 & 0 \\ 0 & 0 & 0 & 0 \\ 0 & 0 & e^{h_+} \cosh h_\times & \sin \theta \sinh h_\times \\ 0 & 0 & \sin \theta \sinh h_\times & e^{-h_+} \cosh h_\times \sin \theta^2 \end{pmatrix}. \quad (5.7)$$

\mathring{R} , h_+ , and h_\times are the three independent quantities contained in $g_{\mu\nu}$. h_+ and h_\times are the propagating degrees of freedom of the GWs manifest in the curvature, i.e. the quantities we measure on Earth, and \mathring{R} is related to the determinant of $g_{\mu\nu}$.

To determine the inverse of the 2-metric, we use the following ansatz

$$q^{\mu\nu} = \begin{pmatrix} f1(T, R, \theta, \phi) & f2(T, R, \theta, \phi) & f5(T, R, \theta, \phi) & f6(T, R, \theta, \phi) \\ f3(T, R, \theta, \phi) & f4(T, R, \theta, \phi) & f7(T, R, \theta, \phi) & f8(T, R, \theta, \phi) \\ f5(T, R, \theta, \phi) & f7(T, R, \theta, \phi) & e^{-h_+} \cosh h_\times & -\csc \theta \sinh h_\times \\ f6(T, R, \theta, \phi) & f8(T, R, \theta, \phi) & -\csc \theta \sinh h_\times & e^{h_+} \cosh h_\times \csc \theta^2 \end{pmatrix}, \quad (5.8)$$

where the f 's are arbitrary functions of the coordinates.

We use the fact that η_μ and $\underline{\eta}_\mu$ are null co-vectors, and therefore they are orthogonal to $g^{\mu\nu}$, i.e.

$$g^{\mu\nu} \eta_\mu = 0 \quad \text{and} \quad g^{\mu\nu} \underline{\eta}_\mu = 0, \quad (5.9)$$

to determine the f functions, thus obtaining the components of $g^{\mu\nu}$. Their explicit lengthy expressions are omitted here and included in Appendix A for the sake of clarity. With this, we can at last write both the metric and its inverse, which suffice to define all the geometric quantities, such as the Christoffel symbols and the Riemann tensor.

5.1.2 Linearization

To linearize, we take Minkowski spacetime as the background. An interesting follow-up calculation would be to linearize around different backgrounds, which was not done in this project due to time constraints. We perform the linearization by expressing the variables as the value they take in flat spacetime plus a small, perturbative term

$$C_+ = 1 + \epsilon \delta C_+^R, \quad (5.10a)$$

$$C_- = -1 + \epsilon \delta C_-^R, \quad (5.10b)$$

$$C_A^\pm = 0 + \epsilon \delta C_A^\pm, \quad (5.10c)$$

$$\varphi = 0 + \epsilon \delta \varphi, \quad (5.10d)$$

$$\mathring{R} = R + \epsilon \delta \mathring{R}, \quad (5.10e)$$

$$h_{+, \times} = 0 + \epsilon \delta h_{+, \times} . \quad (5.10f)$$

By substituting these in the metric, and linearizing in the usual way

$$h_{\mu\nu} = \lim_{\epsilon \rightarrow 0} \partial_\epsilon g_{\mu\nu} , \quad (5.11)$$

one obtains the linearized metric. We can also define the linearized Ricci tensor in the same way

$$\tilde{R}_{\mu\nu} = \lim_{\epsilon \rightarrow 0} \partial_\epsilon R_{\mu\nu} . \quad (5.12)$$

If the reader recalls from chapter 2, a useful quantity to define when one works in the linearized theory is $\bar{h}_{\mu\nu}$, introduced in Eq. (2.18). The components of $h_{\mu\nu}$ and $\bar{h}_{\mu\nu}$ are given in Appendix A, which can be written in terms of the variables δC_\pm , δC_A^\pm , $\delta\varphi$, $\delta\dot{R}^{-1}$, and $\delta h_{+, \times}$. Hence, the evolution equations for these variables contain all the physical information of the system.

The background quantities take their flat spacetime value and are denoted with a dot on top. For instance, the flat background metric in spherical coordinates is $\dot{g}_{\mu\nu} = \text{diag}(-1, 1, R^2, R^2 \sin^2 \theta)$.

5.2 Regularization at the origin

In spherical coordinates, the equations contain terms that diverge with $\mathcal{O}(R^{-2})$ and $\mathcal{O}(\sin^{-2} \theta)$. Choosing as evolved variables a proper rescaling of the tensorial quantities, all code variables remain finite [24]. Furthermore, evolved variables need to be sufficiently smooth functions (at least C^2). Let us obtain the conditions that make the evolved variables satisfy these requirements.

Consider a generic 2-tensor $g_{\mu\nu}$ in Cartesian coordinates

$$g_{\mu\nu} = \begin{pmatrix} g_{TT} & g_{TX} & g_{TY} & g_{TZ} \\ g_{XT} & g_{XX} & g_{XY} & g_{XZ} \\ g_{YT} & g_{YX} & g_{YY} & g_{YZ} \\ g_{ZT} & g_{ZX} & g_{ZY} & g_{ZZ} \end{pmatrix} , \quad (5.13)$$

which is well-defined at the origin. We wish to perform a coordinate transformation – to spherical polar coordinates – in such a way that it remains well-defined near the origin. In terms of spherical polars (T, R, θ, ϕ) , Cartesian coordinates read

$$T = T , \quad (5.14a)$$

$$X = R \sin \theta \cos \phi , \quad (5.14b)$$

$$Y = R \sin \theta \sin \phi , \quad (5.14c)$$

$$Z = R \cos \theta . \quad (5.14d)$$

Hence, the jacobian matrix is defined as

$$J_{\mu'}^{\mu} = \begin{pmatrix} 1 & 0 & 0 & 0 \\ 0 & \cos(\phi) \sin(\theta) & R \cos(\phi) \cos(\theta) & -R \sin(\phi) \sin(\theta) \\ 0 & \sin(\phi) \sin(\theta) & R \cos(\theta) \sin(\phi) & R \cos(\phi) \sin(\theta) \\ 0 & \cos(\theta) & -R \sin(\theta) & 0 \end{pmatrix}. \quad (5.15)$$

In the new coordinates, the components of the tensor $g_{\mu'\nu'}$ can be computed in the following way

$$g_{\mu'\nu'} = J_{\mu'}^{\mu} g_{\mu\nu} J_{\nu'}^{\nu}. \quad (5.16)$$

At the origin, $R = 0$, all angles are the same point physically. Thus, g_{RR} must be independent of the angles θ , ϕ , and the limits in different directions must be the same. In particular, we have that

$$\lim_{\theta \rightarrow 0} g_{RR} = \lim_{\substack{\theta \rightarrow \frac{\pi}{2} \\ \phi \rightarrow 0}} g_{RR} = \lim_{\substack{\theta \rightarrow \frac{\pi}{2} \\ \phi \rightarrow \frac{\pi}{2}}} g_{RR} \implies g_{XX} = g_{YY} = g_{ZZ} := g_{RR}^0. \quad (5.17)$$

On the other hand,

$$\lim_{\theta \rightarrow \frac{\pi}{2}} g_{RR} = g_{RR}^0 + g_{XY} \sin(2\phi), \quad (5.18)$$

but this must not depend on either θ or ϕ . This implies that $g_{XY} = 0$. Similarly, we have that $g_{XZ} = g_{YZ} = 0$.

Proceeding in a similar manner for the g_{TR} component, we conclude that $g_{TX} = g_{TY} = g_{TZ} := g_{TR}^0$. The component g_{TR} is then given by

$$g_{TR} = g_{TR}^0 (\cos \theta + (\cos \phi + \sin \phi) \sin \theta), \quad (5.19)$$

implying that we must have $g_{TR}^0 = 0$.

The generic 2-tensor in spherical polar coordinates at the origin then reads

$$g_{\mu'\nu'} = \text{diag}(g_{TT}, g_{RR}^0, g_{RR}^0 R^2, g_{RR}^0 R^2 \sin^2 \theta). \quad (5.20)$$

To understand how each of the tensor components in spherical coordinates scales with R , we expand it around the origin and impose that derivatives of the tensor components are well-defined functions at the origin, i.e. they must take the same limit independently of the direction we approach the origin from (be it the x-axis, y-axis, z-axis, or any other direction). We start by expanding only up to first-order and determine whether the first derivatives vanish at the origin, e.g.

$$g_{XX} \approx g_{RR}^0 + X \partial_X g_{XX} + Y \partial_Y g_{XX} + Z \partial_Z g_{XX}. \quad (5.21)$$

Let us focus on g_{RR} . If we approach the origin from the x-axis, for instance, we have $y = z = 0$ and $R = x$. Thus, in this situation

$$\partial_R g_{RR} \approx \partial_x g_{RR}. \quad (5.22)$$

The same applies to the other axes. These conditions imply

$$\partial_R g_{RR} \approx \partial_R g_{RR} (\cos \theta + (\cos \phi + \sin \phi) \sin \theta). \quad (5.23)$$

Since this is not allowed to be a function of the angles, we must have that the first radial derivative of the RR component vanishes, $\partial_R g_{RR} = 0$.

Looking at the components $g_{\theta\theta}$ and $g_{\phi\phi}$, and following a similar procedure, we conclude that $\partial_R g_{\theta\theta} = \partial_R g_{\phi\phi} = 0$. Hence we conclude that the expansion of the spatial part of the tensor at the origin is, up to first-order in R , given by Eq. (5.20).

Let us now consider the shift (g_{TX}, g_{TY}, g_{TZ}) . As we saw, it is zero at the origin, so the expansion to first-order includes only the first-order terms:

$$g_{TX} \approx X \partial_X g_{TX} + Y \partial_Y g_{TX} + Z \partial_Z g_{TX}, \quad (5.24a)$$

$$g_{TY} \approx X \partial_X g_{TY} + Y \partial_Y g_{TY} + Z \partial_Z g_{TY}, \quad (5.24b)$$

$$g_{TZ} \approx X \partial_X g_{TZ} + Y \partial_Y g_{TZ} + Z \partial_Z g_{TZ}. \quad (5.24c)$$

Following a similar approach to what was done for the spatial components of $g_{\mu'\nu'}$, we conclude that the expansion of the shift in spherical polars is, up to first-order, given by $(\partial_R g_{TR}, 0, 0)$. An analogous result is obtained for a generic vector.

As we saw, the first-order derivatives of the spatial components vanish, therefore we need to expand to second-order if we want to have more information about their behavior near the origin. By doing the same as for the first derivatives, we conclude that the second derivatives are well-defined near the origin. Thus, a generic tensor can be expressed near the origin in spherical polar coordinates as

$$g_{\mu'\nu'} = \text{diag}(g_{TT}, g_{RR}^0 + \frac{1}{2} \partial_r^2 g_{RR} R^2, g_{RR}^0 R^2 + \frac{1}{2} \partial_r^2 g_{\theta\theta} R^4, g_{RR}^0 R^2 \sin^2 \theta + \frac{1}{2} \partial_r^2 g_{\theta\theta} R^4 \sin^2 \theta), \quad (5.25)$$

where the derivatives are computed at the origin.

In other words, g_{TT} and g_{RR} are even functions and the following conditions must be satisfied

$$\begin{aligned} g_{TR} &= \mathcal{O}(R), \quad g_{T\theta} = \mathcal{O}(R^2), \quad g_{T\phi} = \mathcal{O}(R^2), \quad g_{RR} - \frac{g_{\theta\theta}}{R^2} = \mathcal{O}(R^2), \\ g_{RR} - \frac{g_{\phi\phi}}{R^2 \sin^2 \theta} &= \mathcal{O}(R^2), \quad g_{\theta\phi} = \mathcal{O}(R^3), \quad g_{R\theta} = \mathcal{O}(R^3), \quad g_{R\phi} = \mathcal{O}(R^3). \end{aligned} \quad (5.26)$$

The regularity conditions in terms of our variables imply that, at the origin, the following conditions

must be satisfied

$$\begin{aligned}
\frac{\delta \dot{R}}{R} &= \mathcal{O}(1) + \mathcal{O}(R^2), & \partial_R \delta C_-^R &= \partial_R \delta C_+^R, \\
\delta C_+^R + \delta C_-^R &= \mathcal{O}(R), & \delta C_\theta^- - \delta C_\theta^+ &= \mathcal{O}(R), \\
\delta C_\phi^- - \delta C_\phi^+ &= \mathcal{O}(R), & \delta C_\theta^- + \delta C_\theta^+ &= \mathcal{O}(R^2), \\
\delta C_\phi^- + \delta C_\phi^+ &= \mathcal{O}(R^2), & \delta h_+ &= \mathcal{O}(R^2), \\
\delta \varphi + \frac{1}{2}(\delta C_-^R - \delta C_+^R) &= \mathcal{O}(1) + \mathcal{O}(R^2), & \delta h_\times &= \mathcal{O}(R).
\end{aligned} \tag{5.27}$$

5.3 Regularization at future null infinity

We follow the approach taken in [25] and [26] to regularize the evolution equations at future null infinity. To do so, we come back to the model introduced in chapter 3, the GBU model. Since we are only interested in *good* and *ugly* fields – recall that the *bad* equation had a non-linear term and thus it does not appear in the linearized equations – we will focus only on the good-ugly (GU) equations

$$\square g = S_g(T, R, \theta, \phi), \tag{5.28a}$$

$$\square u - \frac{2}{\chi(R)} \nabla_T u = S_u(T, R, \theta, \phi), \tag{5.28b}$$

with

$$\lim_{R \rightarrow \infty} \chi(R) = R. \tag{5.29}$$

For the purpose of this section, we take $\chi(R) = R$ since we are only interested in the asymptotic behavior. For the numerical implementation, it will be important to redefine $\chi(R)$ as an even function so that *ugly* fields are, like a solution to the wave equation, even. However, in the context of the asymptotic regime, the parity of the fields can be ignored. Furthermore, we consider source terms S_g and S_u . We assume that the source terms decay much faster than the fields – at least like $\mathcal{O}(R^{-3})$ – so that, in the asymptotic regime, the equations approach Eqs. (3.9a) and (3.9c), respectively.

In order to allow for implementations with pseudo-spectral methods, we perform a first-order reduction, i.e. we define new evolved variables as a combination of first-order derivatives of the fields such that we get an equivalent system of equations with only first-order derivatives. For *good* fields, we define

$$g^+ := \partial_T g + \partial_R g, \tag{5.30a}$$

$$g^- := \partial_T g - \partial_R g, \tag{5.30b}$$

$$g_A := \partial_A g, \quad (5.30c)$$

where g^+ and g^- are simply the good and bad derivatives of g , respectively, and similarly for *ugly* fields.

Hence, Eq. (5.28a) can be expressed as the system of equations

$$\partial_T g = \frac{1}{2}(g^+ + g^-), \quad (5.31a)$$

$$\partial_T g^+ = -S_g + \frac{1}{R}(g^+ - g^-) + \frac{1}{R^2} \mathcal{D}^A g_A + \partial_R g^+, \quad (5.31b)$$

$$\partial_T g^- = -S_g + \frac{1}{R}(g^+ - g^-) + \frac{1}{R^2} \mathcal{D}^A g_A - \partial_R g^-, \quad (5.31c)$$

$$\partial_T g_A = \frac{1}{2} \partial_A (g^+ + g^-), \quad (5.31d)$$

where

$$\mathcal{D}^A \psi_A = \frac{1}{\sqrt{g}} \partial_A (\sqrt{g} g^{AB} \psi_B) \quad (5.32)$$

is the divergence on the 2-sphere, and Eq. (5.28b) can be expressed as

$$\partial_T u = \frac{1}{2}(u^+ + u^-), \quad (5.33a)$$

$$\partial_T u^+ = -S_u - \frac{2}{R} u^- + \frac{1}{R^2} \mathcal{D}^A u_A + \partial_R u^+, \quad (5.33b)$$

$$\partial_T u^- = -S_u - \frac{2}{R} u^- + \frac{1}{R^2} \mathcal{D}^A u_A - \partial_R u^-, \quad (5.33c)$$

$$\partial_T u_A = \frac{1}{2} \partial_A (u^+ + u^-). \quad (5.33d)$$

After performing the hyperboloidal compactification, we get

$$\partial_t g = \frac{1}{2}(g^+ + g^-), \quad (5.34a)$$

$$\partial_t g^+ = -\frac{S_g}{1+H'} + \frac{g^+ - g^-}{R(1+H')} + \frac{\mathcal{D}^A g_A}{R^2(1+H')} + \frac{\partial_r g^+}{R'(1+H')}, \quad (5.34b)$$

$$\partial_t g^- = \frac{S_g}{-1+H'} - \frac{g^+ - g^-}{R(-1+H')} - \frac{\mathcal{D}^A g_A}{R^2(-1+H')} + \frac{\partial_r g^-}{R'(-1+H')}, \quad (5.34c)$$

$$\partial_t g_A = \frac{1}{2} \partial_A (g^+ + g^-), \quad (5.34d)$$

and

$$\partial_t u = \frac{1}{2}(u^+ + u^-), \quad (5.35a)$$

$$\partial_t u^+ = -\frac{S_u}{1+H'} - \frac{2u^-}{R(1+H')} + \frac{\mathcal{D}^A u_A}{R^2(1+H')} + \frac{\partial_r u^+}{R'(1+H')}, \quad (5.35b)$$

$$\partial_t u^- = \frac{S_u}{-1 + H'} + \frac{2u^-}{R(-1 + H')} - \frac{\mathcal{D}^A u_A}{R^2(-1 + H')} + \frac{\partial_r u^-}{R'(-1 + H')}, \quad (5.35c)$$

$$\partial_t u_A = \frac{1}{2} \partial_A (u^+ + u^-), \quad (5.35d)$$

where $H \equiv H(R(r))$ is the height function defined in chapter 3. For these equations to be numerically regular at future null infinity, the coefficients must be at most $\mathcal{O}(1)$. We demand that $H' = 1 - R'^{-1}$, and choose R such that $R' \sim \mathcal{O}(R^2)$. Note that the source terms, S_g and S_u , must decay at least like $\mathcal{O}(R^{-2})$ in order for the first term on the right-hand side (RHS) to be regular. The coefficient in the second term of the RHS of Eqs. (5.34c) and (5.35c) is $\mathcal{O}(R)$ and therefore these equations are not regular at \mathcal{I}^+ . We can redefine our evolved variables to include such diverging terms. Therefore, we introduce the rescaled fields

$$G = \chi(R)g, \quad (5.36a)$$

$$G^+ = \chi(R)(\chi(R)g)^+, \quad (5.36b)$$

$$G^- = \chi(R)g^-, \quad (5.36c)$$

$$G_A = \chi(R)\tilde{\partial}_A g, \quad (5.36d)$$

where $\tilde{\partial}_A = (\partial_\theta, \frac{1}{\sin(\theta)}\partial_\phi)^T$. Analogously, we introduce rescaled fields for u . In the asymptotic regime, the equations become

$$\partial_t G \simeq \frac{1}{2}G^- - \frac{1}{2R}G + \frac{1}{2R}G^+, \quad (5.37a)$$

$$\partial_t G^+ \simeq -c_-^r G^+ - \mathcal{A}^- \mathcal{D}^A G_A + S_{G^+} \quad (5.37b)$$

$$\partial_t G^- \simeq -c_-^r \partial_r G^- + \mathcal{A}^+ \mathcal{D}^A G_A + S_{G^-} \quad (5.37c)$$

$$\partial_t G_A \simeq \frac{\tilde{\partial}_A G^+}{2R} + \frac{1}{2}\tilde{\partial}_A G^- - \frac{G_A}{2R}, \quad (5.37d)$$

and

$$\partial_t U \simeq \frac{1}{2}U^- - \frac{1}{2R}U + \frac{1}{2R}U^+, \quad (5.38a)$$

$$\partial_t U^+ \simeq -c_-^r U^+ - \mathcal{A}^- \mathcal{D}^A U_A + S_{U^+}, \quad (5.38b)$$

$$\partial_t U^- \simeq -c_+^r \partial_r U^- + \mathcal{A}^+ \mathcal{D}^A U_A + S_{U^-}, \quad (5.38c)$$

$$\partial_t U_A \simeq \frac{\tilde{\partial}_A U^+}{2R} + \frac{1}{2}\tilde{\partial}_A U^- - \frac{U_A}{2R}, \quad (5.38d)$$

where we have introduced the following quantities

$$\alpha_+ = 1, \quad (5.39a)$$

$$\alpha_- = \chi, \quad (5.39b)$$

$$c_\pm^r = \frac{\pm 1}{(1 \mp H')R'}, \quad (5.39c)$$

$$\mathcal{A}^\pm = \frac{R'}{R} \alpha_\pm c_\pm^r. \quad (5.39d)$$

The lower-order terms contained in S_{G^+} , S_{G^-} , S_{U^+} , S_{U^-} are explicitly given in Appendix B.

Besides making the equations numerically more regular at \mathcal{I}^+ , this choice of evolved variables is appropriate since it allows us to extract the radiation fields directly.

5.4 Model equations

Recall the ten independent metric components δC_\pm , δC_A^\pm , $\delta\varphi$, $\delta\dot{R}^{-1}$, and $\delta h_{+,\times}$, whose evolution accommodates the physical information of the system. In section 3.4, we said that two of these – $\delta h_{+,\times}$ – behave like a solution to the wave equation. Hence, they will be modeled as *goods*, whereas the other eight fields, which decay faster asymptotically, will be modeled as *uglies*. We are thus looking to have two equations of the form of Eq. (5.28a) and eight of the form of Eq. (5.28b).

Alternatively, since we have that $T^a = \frac{1}{2}(\xi^a + \underline{\xi}^a)$, the *ugly* equation can be expressed in the form

$$\square_1 u := \square u - R^{-1} \nabla_\xi u = \tilde{S}_u, \quad (5.40)$$

where $\tilde{S}_u = S_u + \nabla_\xi u$.

The appropriate rate of decay of the fields can be imposed, i.e. we can force the eight *ugly* equations to have the form of Eq. (5.40), through gauge fixing and constraint addition.

5.4.1 Generalized Harmonic Gauge

As discussed in chapter 2, there is still gauge freedom left after we linearize GR. In that chapter, we introduced the harmonic gauge, which is a common choice since it leads to wave equations. In this work, we impose a generalization of this gauge – the Generalized Harmonic Gauge (GHG) – that not only leads to well-posed equations but also allows us to impose the rate of decay of the fields such that they attain a non-vanishing finite limit at future null infinity.

In GHG, instead of setting the divergence of $\bar{h}_{\mu\nu}$ to zero, we set it to some arbitrary functions of the coordinates

$$\nabla^\nu \bar{h}_{\mu\nu} + F_\mu = 0. \quad (5.41)$$

These functions can be used to impose the rate of decay of four of the fields. We also define a harmonic constraint equal to the quantity above,

$$Z_\mu \equiv \nabla^\nu \bar{h}_{\mu\nu} + F_\mu, \quad (5.42)$$

which is used to impose conditions on four other fields.

For our setup, these constraints have components

$$Z_\xi = \nabla_\xi \delta C_+^R - \frac{2}{R} \delta C_+^R + 2R \nabla_\xi \delta \dot{R}^{-1} + 6\delta \dot{R}^{-1} + \frac{2}{R} \delta \varphi - \mathcal{D}^A \delta C_A^+ + F_\xi, \quad (5.43a)$$

$$Z_\xi = -\nabla_\xi \delta C_-^R - \frac{2}{R} \delta C_-^R + 2R \nabla_\xi \delta \dot{R}^{-1} - 6\delta \dot{R}^{-1} - \frac{2}{R} \delta \varphi + \mathcal{D}^A \delta C_A^- + F_\xi, \quad (5.43b)$$

$$Z_A = RF_A - \frac{3}{2}(\delta C_A^+ + \delta C_A^-) + \frac{R}{2}(\nabla_\xi \delta C_A^+ - \nabla_\xi \delta C_A^-) + \mathcal{D}^B \hat{h}_{AB} - \partial_A \delta \varphi. \quad (5.43c)$$

We define a new linearized Ricci tensor

$$\delta \mathcal{R}_{\mu\nu} \equiv \delta R_{\mu\nu} - \nabla_{(\mu} Z_{\nu)} + W_{\mu\nu}, \quad (5.44)$$

where the second term cancels the terms in the linearized Ricci tensor that are not the wave operator and $W_{\mu\nu}$ is a sparse matrix with components that depend only on the harmonic constraint. The evolution equations are obtained by making the appropriate contractions with $\delta \mathcal{R}_{\mu\nu}$. For instance, the Equation of Motion (EOM) for δC_+^R is obtained by

$$\xi^\mu \xi^\nu \delta \mathcal{R}_{\mu\nu} = 0. \quad (5.45)$$

The remaining seven *ugly* equations are obtained by making the following contractions: $\xi^\mu \mathcal{R}_{\mu A}$, $\mathcal{G}^{\mu\nu} \mathcal{R}_{\mu\nu}$, $\xi^\mu \xi^\nu \mathcal{R}_{\mu\nu}$, $\xi^\mu \mathcal{R}_{\mu A}$, $\xi^\mu \xi^\nu \mathcal{R}_{\mu\nu}$. The resulting EOMs follow

$$\square_1 \delta C_+^R = R^{-1} \nabla_\xi (2R \delta \dot{R}^{-1} + RF_\xi) + \mathcal{D}^A \delta C_A^+, \quad (5.46a)$$

$$\square_1 \delta C_A^+ = -2R^{-2} \nabla^B \hat{h}_{AB} + 2R^{-2} (\delta C_A^+ + \delta C_A^- - F_A) + R^{-1} \nabla_\xi (F_A - \delta C_A^+) + R^{-1} \partial_A (F_\xi + 4\delta \dot{R}^{-1} + 2R^{-1} \delta \varphi - 2R^{-1} \delta C_+^R), \quad (5.46b)$$

$$\square_1 \delta \dot{R}^{-1} = \frac{F_\xi - F_\xi}{2R^2} + \frac{\delta \varphi}{R^3} - \frac{\nabla_\xi \delta \dot{R}^{-1}}{R} + \frac{\delta C_-^R - \delta C_+^R}{2R^3} + \mathcal{D}^A (\delta C_A^+ + \delta C_A^- - \delta F_A), \quad (5.46c)$$

$$\square \delta C_-^R + \nabla_\xi F_\xi = \frac{2\delta C_-^R}{R^2} + \frac{2\delta\varphi}{R^2} + \frac{4\delta\dot{R}^{-1}}{R} - 2\mathcal{D}^A \delta C_A^-, \quad (5.46d)$$

$$\begin{aligned} \square_1 \delta C_A^- = & -\frac{\delta C_A^- + \delta C_A^+}{R^2} + \frac{\nabla_\xi(\delta C_A^+ - F_A)}{R} - \frac{2\nabla_\xi \delta C_A^-}{R} \\ & + \partial_A \left(\frac{2\delta C_-^R}{R^2} - \frac{F_\xi}{R} + \frac{4\delta\dot{R}^{-1}}{R} \right) - \frac{1}{R} Z_A, \end{aligned} \quad (5.46e)$$

$$\square \delta\varphi - \frac{1}{2} \nabla_\xi F_\xi = \frac{2\delta\varphi}{R^2} + \frac{4\delta\dot{R}^{-1}}{R} + \frac{1}{2} \nabla_\xi F_\xi + \frac{\delta C_-^R - \delta C_+^R}{R^2} + \mathcal{D}^A (\delta C_A^+ + \delta C_A^-). \quad (5.46f)$$

$$(5.46g)$$

The *good* equations are straightforward to obtain. We define the projected linearized metric on the background 2-sphere

$$\hat{h}_{\mu\nu} = \perp_{\mu\nu}{}^{\alpha\beta} h_{\alpha\beta}, \quad (5.47)$$

where the projection operator is given by

$$\perp_{\mu\nu}{}^{\alpha\beta} = (\dot{g}_{(\mu}{}^\alpha \dot{g}_{\nu)}{}^\beta - \frac{1}{2} \dot{g}_{\mu\nu} \dot{g}^{\alpha\beta}), \quad (5.48)$$

and applying the D'Alembert operator we get

$$\square \hat{h}_{AB} = 2 \perp_{AB}{}^{ab} \mathcal{D}_{(a} (\delta C_{|b)}^+ + \delta C_{|b)}^- - F_{|b)}) + M_{AB} \mathcal{D}_a (\delta C_+^{R,a} + \delta C_-^{R,a}), \quad (5.49)$$

where

$$M_{AB} = \begin{pmatrix} 1 & 0 \\ 0 & -1 \end{pmatrix}. \quad (5.50)$$

Recall that we can choose the gauge source functions to make four fields be modeled as *uglies*, namely δC_-^R , δC_A^- , and $\delta\varphi$. The choice that satisfies this requirement is

$$F_\xi = \frac{\delta\varphi}{R}, \quad F_\xi = -\frac{\delta C_-^R}{R}, \quad F_A = \delta C_A^+. \quad (5.51)$$

With this choice, the equations yield

$$\square_1 \delta C_+^R = 2R^{-1} \nabla_\xi (R \delta\dot{R}^{-1} + \delta\varphi) + \mathcal{D}^A \delta C_A^+, \quad (5.52a)$$

$$\square_1 \delta C_A^+ = -\frac{2}{R^2} \nabla^B \hat{h}_{AB} + \frac{2\delta C_A^+}{R^2} + \frac{4\partial_A \delta\dot{R}^{-1}}{R} + \frac{4\partial_A \delta\varphi}{R^2} - \frac{2\partial_A \delta C_+^R}{R^2}, \quad (5.52b)$$

$$\square_1 \delta\dot{R}^{-1} = \frac{2\delta\varphi}{R^3} + \frac{\delta C_-^R}{2R^3} - \frac{\nabla_\xi \delta\dot{R}^{-1}}{R} + \frac{\delta C_-^R}{2R^3} - \frac{\delta C_+^R}{2R^3} + \mathcal{D}^A \delta C_A^-, \quad (5.52c)$$

$$\square_1 \delta C_-^R = \frac{3\delta C_-^R}{R^2} + \frac{2\delta\varphi}{R^2} + \frac{4\delta\dot{R}^{-1}}{R} - 2\mathcal{D}^A \delta C_A^-, \quad (5.52d)$$

$$\square_1 \delta C_A^- = \frac{3\partial_A \delta C_-^R}{R^2} - \frac{\delta C_A^-}{R^2} - \frac{\delta C_A^+}{R^2} + \frac{4\partial_A \delta \dot{R}^{-1}}{R} - \frac{2\nabla_\xi \delta C_A^-}{R} - \frac{1}{R} Z_A, \quad (5.52e)$$

$$\square_1 \delta \varphi = \frac{2\delta \varphi}{R^2} + \frac{4\delta \dot{R}^{-1}}{R} - \frac{1}{2} \nabla_\xi \frac{\delta C_-^R}{R} + \frac{\delta C_-^R - \delta C_+^R}{R^2} + \mathcal{D}^A (\delta C_A^+ + \delta C_A^-), \quad (5.52f)$$

$$\square \hat{h}_{AB} = 2 \perp_{AB}^{ab} \mathcal{V}_{(a|} \delta C_{|b)}^- + M_{AB} \mathcal{V}_a (\delta C_+^{R,a} + \delta C_-^{R,a}). \quad (5.52g)$$

These equations have the form we expected them to have, (5.40) for eight of the fields and (5.28a) for the propagating degrees of freedom, with RHSs $\sim \mathcal{O}(R^{-3})$. This proves that the linearized Einstein equations can indeed be modeled by the GU model.

5.4.2 Transverse-Traceless gauge

Let us now compare our gauge with the usual TT gauge. In TT gauge we have that

$$h^{TT} = 0, \quad \bar{h}_{0\mu}^{TT} = 0. \quad (5.53)$$

These conditions must be satisfied by the initial data, at $t = 0$, and later. Thus, in terms of our variables, the conditions above translate to

$$\delta C_+^R = -\delta C_-^R, \quad (5.54a)$$

$$\delta C_A^+ = \delta C_A^-, \quad (5.54b)$$

$$\delta \dot{R}^{-1} = \frac{\delta C_-^R}{2R}, \quad (5.54c)$$

$$\delta \varphi = \delta C_-^R, \quad (5.54d)$$

and a similar relation for the time derivatives of the fields. By considering these relations, and choosing the gauge source functions to be zero, we see that equations for the dependent variables turn out to be the same as the EOMs for the independent variables, indicating that if we impose TT gauge for the initial data, it gets propagated.

6

Numerical simulations

Contents

6.1	NRPy+	44
6.2	Implemented equations	44
6.3	Boundary Condititons	45
6.4	Numerical treatment of the origin	47
6.5	Initial Data	47
6.6	Results	48

In this chapter, we start by introducing the tools we worked with. Then, we explain the numerical implementation and present the results obtained. The code developed is available [here](#), as well as the Mathematica notebooks used to make the plots.

6.1 NRPy+

NRPy+ is a collection of Python scripts that generates optimized code in C and is mostly used for solving problems in NR. It can be obtained using Git via the command

```
$ git clone https://github.com/zachetienne/nrpytutorial.git
```

The first paper on NRPy+ was released on December 2017 [27]. Since then, NRPy+ has been continuously updated with new features, and an improved version is expected to be available soon.

The NRPy+ package comes with several helpful [tutorials](#). For our problem, in particular, the most relevant tutorial is *Tutorial-Start_to_Finish-ScalarWaveCurvilinear.ipynb*, which allows us to solve the scalar wave equation in spherical coordinates. Taking advantage of this code, we modified it to solve our equations in the hyperboloidal setting.

6.2 Implemented equations

For the numerical implementation, we perform the hyperboloidal compactification, as explained in chapter 3, and choose

$$R(r) = \frac{r}{1-r}, \quad (6.1)$$

where r is the compactified radial coordinate, so that \mathcal{I}^+ corresponds to the point at $r = 1$, and set the height function to

$$H(r) = R(r) - r. \quad (6.2)$$

For the rescaling function $\chi(R)$, introduced in chapter 5, we choose

$$\chi(R) = \sqrt{1+R^2}, \quad (6.3)$$

so that it is an even function that does not vanish at the origin and approaches R asymptotically. Therefore, in the asymptotic limit we recover Eqs. (5.37) and (5.38).

We set the source terms S_g and S_u to zero. In the future, we could expand this work by considering non-vanishing source terms.

The implemented equations read

$$\partial_t G = \frac{1}{2}G^- - \frac{R}{2\chi^2}G + \frac{1}{2\chi}G^+, \quad (6.4a)$$

$$\partial_t G^+ = -c_-^r G^+ - \mathcal{A}^- \mathcal{B}^A G_A + S_{G^+}, \quad (6.4b)$$

$$\partial_t G^- = -c_-^r \partial_r G^- + \mathcal{A}^+ \mathcal{B}^A G_A + S_{G^-}, \quad (6.4c)$$

$$\partial_t G_A = \frac{\tilde{\partial}_A G^+}{2\chi} + \frac{1}{2}\tilde{\partial}_A G^- - \frac{R}{2\chi^2}G_A, \quad (6.4d)$$

$$\partial_t U = \frac{1}{2}U^- - \frac{R}{2\chi^2}U + \frac{1}{2\chi}U^+, \quad (6.4e)$$

$$\partial_t U^+ = -c_-^r U^+ - \mathcal{A}^- \mathcal{B}^A U_A + S_{U^+}, \quad (6.4f)$$

$$\partial_t U^- = -c_+^r \partial_r U^- + \mathcal{A}^+ \mathcal{B}^A U_A + S_{U^-}, \quad (6.4g)$$

$$\partial_t U_A = \frac{\tilde{\partial}_A U^+}{2\chi} + \frac{1}{2}\tilde{\partial}_A U^- - \frac{R}{2\chi^2}U_A, \quad (6.4h)$$

where the notation of section 5.3 is used. We also define the constraints

$$\frac{-1}{\chi}\Psi^+ + \frac{1}{2R'-1}\left(\Psi^- - \frac{\chi'}{\chi}\Psi + 2\partial_r\Psi\right) = 0, \quad (6.5)$$

$$\Psi_A - \tilde{\partial}_A\Psi = 0, \quad (6.6)$$

where $\Psi = G, U$, and check that they are satisfied during the evolution.

The method of lines is employed for time integration and is performed with a fourth-order accurate Runge-Kutta scheme. Second-order centered finite differences are used to approximate spatial derivatives. We add Kreiss-Oliger dissipation [28] to our equations, which consists of adding a term to the RHSs of the form

$$\sigma(\Delta x)^3 D_+^2 D_-^2 \psi / 16, \quad (6.7)$$

where σ is the dissipation strength, Δx is the grid spacing, D_\pm the standard forward and backward differencing operators and ψ stands for a field. For our simulations in axial symmetry, we used dissipation strength $\sigma = 0.2$.

We work with a staggered grid, i.e. there are no grid points exactly at the origin and at \mathcal{J}^+ , but they get closer as the resolution is increased.

6.3 Boundary Condititons

Our numerical domain satisfies

$$r \in [0, 1], \quad \theta \in [0, \pi], \quad \phi \in [-\pi, \pi]. \quad (6.8)$$

In spherical coordinates, there are two types of numerical boundaries – inner and outer. To define the boundary conditions, we introduce points that lay beyond the domains defined above and that serve only for numerical purposes, not having any physical meaning – we call them ghost points. These points are distributed into ghost zones, which are like layers. We use two ghost zones, meaning that we extend the grid in every direction by two points. Due to the hyperboloidal compactification we performed, as explained in chapter 3, no outer boundary conditions are needed. However, we do need to fill in the ghost points, which we do via extrapolation. On the other hand, to compute the centered finite difference approximation of the spatial derivatives for the inner grid points, one needs to know the value of the field at the two nearest points. The inner boundary conditions, which map ghost points to other points in the interior of the grid, must then be defined.

Most of the quantities we consider are even, because, since g is a solution to the wave equation, it is even in R as long as we start with an even function of R as initial data. Any derivative that does not involve the radial coordinate is therefore also even, for instance, $\partial_T g$ and $\partial_A g$. Thus, as long as we choose $\chi(R)$ to be an even function of R – which we have – G and G_θ are even. Notice that, for our choice of $R(r)$, (6.1), an even function of R is also an even function of r . An even function of r , ψ , satisfies the inner boundary conditions

$$\psi(r, \theta, \pm\pi \pm \phi) = \psi(r, \theta, \pm\pi \mp \phi), \quad (6.9a)$$

$$\psi(r, -\theta, \phi) = \psi(r, |\theta|, \phi \pm \pi), \quad (6.9b)$$

$$\psi(r, \pi + \theta, \phi) = \psi(r, \pi - \theta, \phi \pm \pi), \quad (6.9c)$$

$$\psi(-r, \theta, \phi) = \psi(r, \pi - \theta, \phi \pm \pi), \quad (6.9d)$$

where in the last three relations the sign in $\phi \pm \pi$ is chosen such that the resulting points lie inside the domain.

However, the parity of the characteristic fields is not as straightforward, since they include radial derivatives of the fields. But, since $\partial_T g$ is even, from the definition of the characteristic fields, we have that $g^+(-R) - \partial_R g(-R) = g^-(R) + \partial_R g(R)$. Writing this in terms of the rescaled fields and in hyperboloidal coordinates, we obtain the parity conditions for G^+ and G^- , which are neither even nor odd,

$$G^+(-r) = \chi(R(r))G^-(r) - \chi'(R(r))G(r), \quad (6.10a)$$

$$G^-(-r) = \frac{G^+(r)}{\chi(R(r))} - \frac{\chi'(R(r))G(r)}{\chi(R(r))}, \quad (6.10b)$$

and similarly for U .

6.4 Numerical treatment of the origin

Our equations have formally singular terms of the form $\frac{2}{r}\psi$. We solve this by applying Evan's method [29], as discussed in [26, 30], which consists of defining a new differencing operator that includes these diverging terms, \tilde{D} . Thus, the system

$$\partial_t \psi = \partial_r \pi, \quad (6.11a)$$

$$\partial_t \pi = \partial_r \psi + \frac{2}{r}\psi, \quad (6.11b)$$

turns into

$$\partial_t \psi = \Delta r^{-1} D \pi, \quad (6.12a)$$

$$\partial_t \pi = \Delta r^{-1} \tilde{D} \psi, \quad (6.12b)$$

where the differencing operators are computed by

$$\tilde{D}\psi = 3 \frac{r_{i+1}^2 \psi_{i+1} - r_{i-1}^2 \psi_{i-1}}{r_{i+1}^3 - r_{i-1}^3}, \quad (6.13a)$$

$$D\pi = \frac{\pi_{i+1} - \pi_{i-1}}{2}. \quad (6.13b)$$

In this way, we avoid diverging terms in the RHSs.

6.5 Initial Data

Initial data must be smooth functions of the coordinates everywhere in the domain. We consider the spherical harmonics,

$$\varphi = \sum_{l=0}^{\infty} \sum_{m=-l}^{m=l} \varphi_{lm}(t, r) Y_{lm}(\theta^A), \quad (6.14)$$

where φ_{lm} is given by

$$\varphi_{lm} = \sum_{k=0}^l \frac{(k+l)!}{2^k k! (l-k)!} \frac{1}{r^{k+1}} [F^{l-k}(u) - (-1)^{l-k} F^{l-k}(v)], \quad (6.15)$$

with $u = t - r$ the retarded time and $v = t + r$ the advanced time.

We make a similar choice for the initial data (at $t = 0$) of G and U , $t = 0$, choosing an axially symmetric expression as in [31], $\varphi_{20} Y_{20}$, where

$$Y_{20} = \frac{1}{4} \sqrt{\frac{5}{\pi}} (3 \cos^2 \theta - 1), \quad (6.16)$$

and we take

$$F(r) = e^{-(r-1/4)^2}. \quad (6.17)$$

The initial data for the other fields are computed straightforwardly by taking the appropriate derivatives and rescalings, in accordance with their definition (5.36).

6.6 Results

In the following, we present the numerical results from the implementation. Since the simulations were performed in axial symmetry, G_ϕ , and U_ϕ are zero everywhere. Thus, they are omitted from this discussion.

The evolution in time of the G and U fields is represented in the top and bottom panels of Fig. 6.1, respectively, in a polar plot with r and θ dependence, where the outer boundary represents \mathcal{I}^+ . We see that the signal in the G evolution leaves the domain completely through \mathcal{I}^+ . Comparatively, we observe that the U signal decays faster, as expected, and that it is always zero at \mathcal{I}^+ . *Ugly* fields decay faster than a solution to the wave equation, i.e. at least like $\mathcal{O}(R^{-3})$. Consequently, even when rescaled by $\chi(R)$ they decay fast enough to vanish at \mathcal{I}^+ .

The basic dynamics of the evolution of the G_θ and U_θ fields are represented in Fig. 6.2. These results albeit similar to the ones above are included here since they constitute a new contribution – as so far, only the spherically symmetric case had been done – namely, the evolution of *ugly* fields in axial symmetry in hyperboloidal coordinates in first-order in space (i.e. with only first-order spatial derivatives). So far, only the spherically symmetric case had been done. We again see that the *ugly* field, U_θ , decays faster than the *good* one, and is always zero at \mathcal{I}^+ , as expected.

The values of the rescaled *good* fields at \mathcal{I}^+ are shown in Fig. 6.3. These were obtained through a fourth-order extrapolation. Fourth-order extrapolation is necessary due to using a staggered grid, that does not have grid points at the extremes. We can see that they are finite for every t and θ , and they approach zero for later times. We omit the G^+ plot here since G^+ is expected to be zero at \mathcal{I}^+ – from the simulations, we obtain values of 2-3 orders of magnitude lower than for the other fields. This is because, by definition,

$$G^+ = \chi(\chi g)^+,$$

and g is a solution to the wave equation, i.e. it decays like $\mathcal{O}(R^{-2})$. Asymptotically, we have that $\chi(R) = R$. Finally, since good derivatives improve the rate of decay of the fields, we conclude that $G^+ \sim \mathcal{O}(R^{-1})$, therefore vanishing at \mathcal{I}^+ . For the same reason, the plots of the values of the *ugly* fields at \mathcal{I}^+ are also omitted here.

To check convergence, the code was first run with 80 grid points in r , 16 in θ and 4 in ϕ , and then the

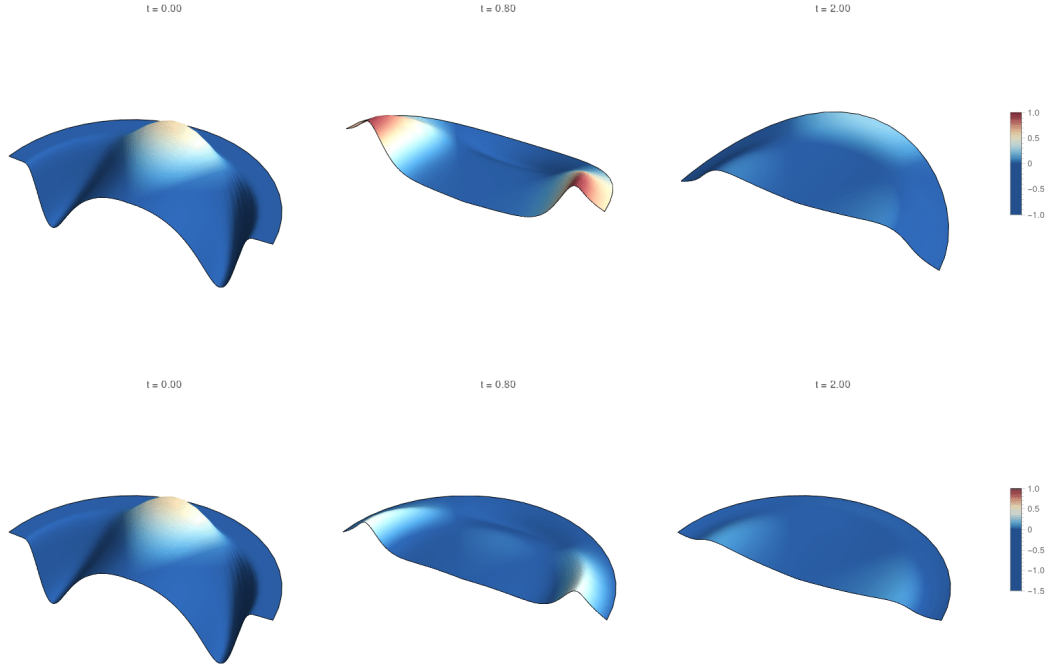


Figure 6.1: Dynamics of the evolution of the G (on top) and U (on the bottom panel) fields in axial symmetry starting with initial data given in Sec. 6.5. The evolution depicted here was performed with 120 grid points in the radial coordinate, 24 grid points in θ , and 4 points in ϕ . Even though we are evolving axially symmetric data, four points in ϕ are needed for the boundary conditions, which have two ghost zones. As expected, the *ugly* fields decay must faster than the *goods*, and are always zero at future null infinity.

resolution in r and θ was iteratively increased by a factor of $p = 1.5$ in the two following runs.

To compute the convergence factor, we considered the energy norm as defined in [32]

$$E(t) = \int_{\Sigma} \varepsilon dr d\Omega, \quad (6.18)$$

with

$$\varepsilon = \frac{1}{2} \left[\left(\frac{2R' - 1}{2R'} \right) (\psi^+)^2 + \left(\frac{1}{2R'} \right) (\psi^-)^2 + \frac{1}{R^2} \psi_\theta^2 + \frac{1}{R^2 \sin \theta} \psi_\phi^2 \right] R^2 R', \quad (6.19)$$

where ψ stands for the fields (*goods* and *uglies*) before being rescaled (see (5.30a)). The convergence factor of the state-vector $(G, G^+, G^-, G^\theta, U, U^+, U^-, U^\theta)$ defined with the norm (6.19) is plotted in Fig. 6.4. We observe that it is roughly 2, as expected for a second-order finite difference approximation (chosen in this experiment), suggesting a successful result.

As explained in chapter 4, we performed pointwise convergence at \mathcal{I}^+ to further ensure the correctness of the results. To do that, we used a fourth-order extrapolation of the *good* fields at future null infinity (recall that the *ugly* fields all vanish at \mathcal{I}^+ , thus this analysis is pointless for those fields). Then we computed the differences between high and medium resolutions and between medium and low. The

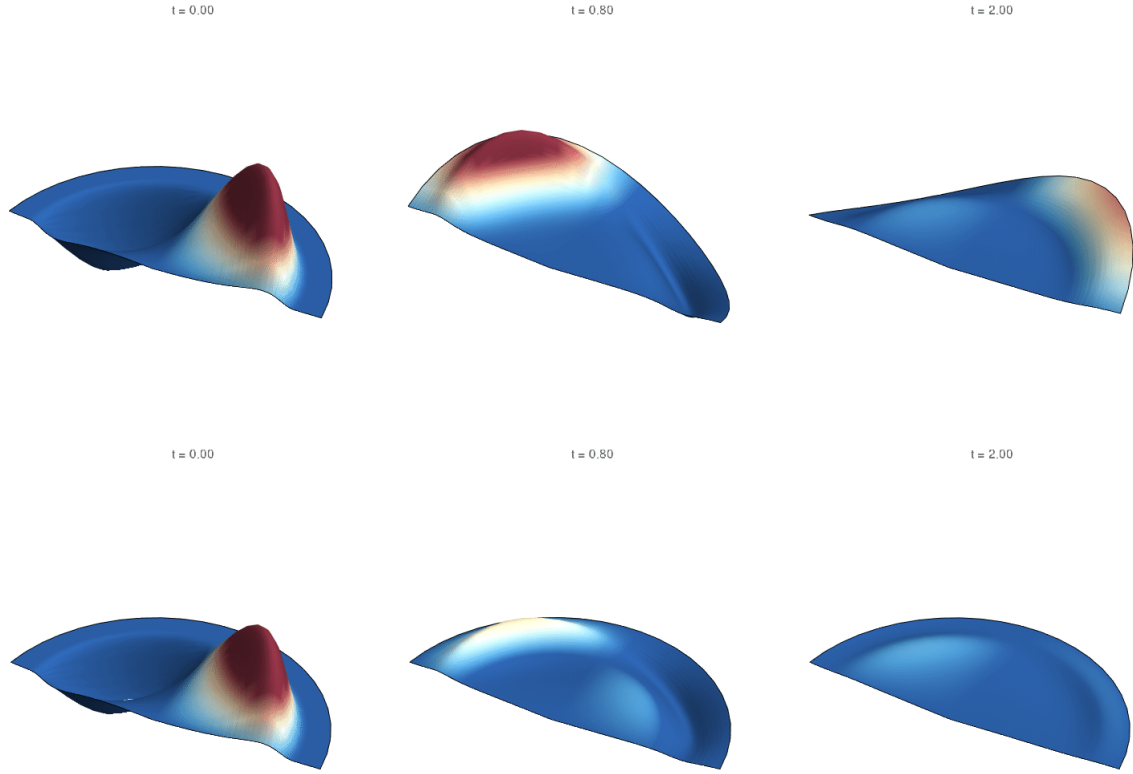


Figure 6.2: Dynamics of the evolution of the G_θ (on top) and U_θ (on the bottom panel) fields in axial symmetry starting with initial data according to Sec. 6.5. The evolution depicted here was performed with 120 grid points in the radial coordinate, 24 grid points in θ , and 4 points in ϕ . Although we are taking an axially symmetric expression for the initial data, we use 4 points in ϕ . Even though we are evolving axially symmetric data, four points in ϕ are needed for the boundary conditions, which have two ghost zones. As expected, the *ugly* fields decay must faster than the *goods*, and are always zero at future null infinity.

latter was rescaled by a factor of 1.5^2 , and the result is plotted in Fig. 6.5. We can see that the rescaled differences align almost perfectly on top of each other, indicating convergence at \mathcal{I}^+ .

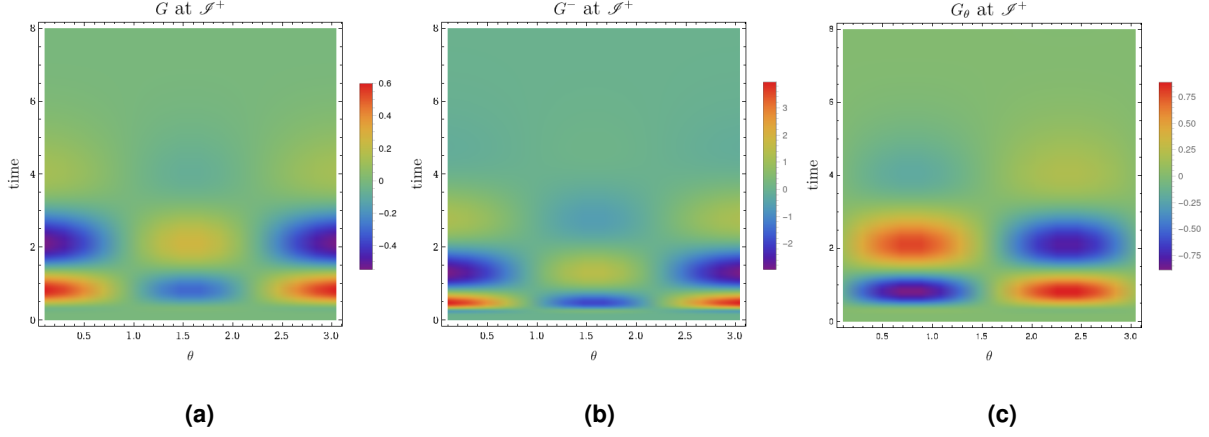


Figure 6.3: Values of the (a) G , (b) G^- , and (c) G_θ fields at \mathcal{S}^+ for all values of time and θ from the evolution with 80 grid points in r , 16 in θ and 4 in ϕ starting with initial data according to Sec. 6.5. Even though we are evolving axially symmetric data, four points in ϕ are needed for the boundary conditions, which have two ghost zones. The values were obtained through a fourth-order extrapolation, necessary due to the centered grid. We notice that for later times the fields vanish, indicating that the signals leave the domain completely through \mathcal{S}^+ .

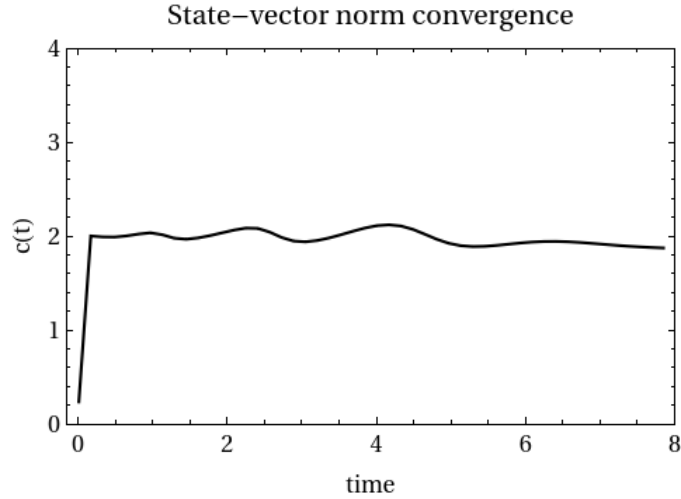
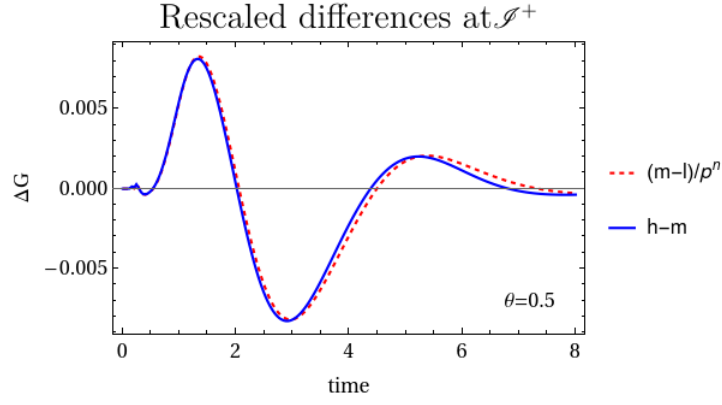
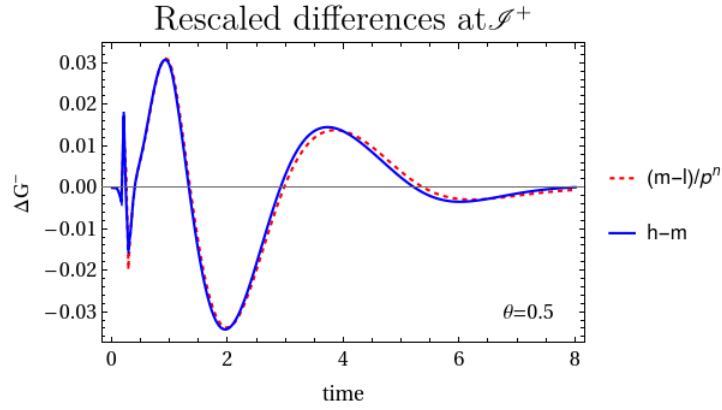


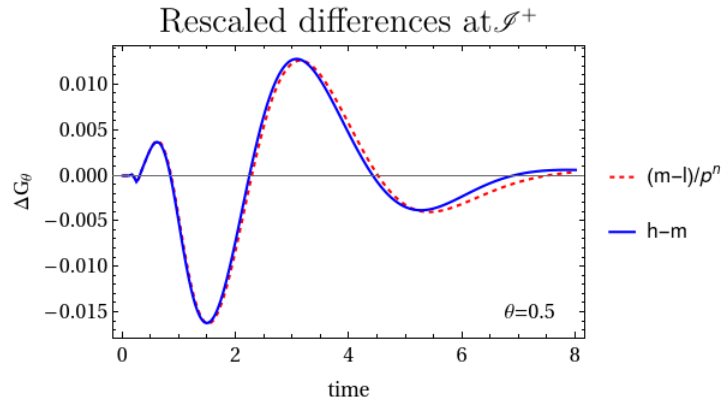
Figure 6.4: Norm convergence of the state-vector ($G, G^+, G^-, G^\theta, U, U^+, U^-, U^\theta$) in axial symmetry with the norm (6.19), starting with 80 grid points in r , 16 in θ and 4 in ϕ and increasing the resolution by a factor of $p = 1.5$. Even though we are evolving axially symmetric data, four points in ϕ are needed for the boundary conditions, which have two ghost zones. We see that the convergence factor approaches 2, as anticipated for second-order finite differences approximation, which indicates a successful result.



(a)



(b)



(c)

Figure 6.5: Rescaled differences at \mathcal{I}^+ with $\theta = 0.5$ for: (a) the G field, (b) the G^- field, and (c) the G_θ field. Starting with 80 grid points in the radial coordinate, 16 in θ and 4 in ϕ , the resolution was increased by a factor of $p = 1.5$. Even though we are evolving axially symmetric data, four points in ϕ are needed for the boundary conditions, which have two ghost zones. The evolution was performed with second-order finite differencing approximation of spatial derivatives, i.e. $n = 2$. l, m, and h stand for the values of the corresponding field given by the low, medium, and high-resolution runs, respectively. The alignment of the rescaled differences indicates convergence at \mathcal{I}^+ .

7

Discussion of the results

Contents

7.1 Summary	54
7.2 Future work	54

7.1 Summary

This work represents a first step toward the implementation of the hyperboloidal approach to solving problems numerically in full GR. This approach will allow for more accurate results than the currently employed methods since it allows for the computation of the GWs all the way out to \mathcal{I}^+ , where they are unambiguously defined, via a smooth slice.

We took the linearized EFE in GHG and, by a careful choice of gauge source functions and constraint additions, showed that linearized GR can be modeled by the GU model, which allows us to understand the rate of decay of the fields and therefore how they should be rescaled such that they attain the expected limit at future null infinity. We also explored how our choice of gauge relates to the usual TT gauge.

By performing a hyperboloidal compactification and properly rescaling the fields, we derived regular equations at future null infinity. In fact, the rescaled fields are the relevant quantities to compute since they are the radiation fields that we measure experimentally.

The regularity conditions at the origin were also derived, and we stress the importance of requiring that the evolved variables be sufficiently smooth functions of the coordinates.

Using NRPy+, the model equations were implemented in hyperboloidal coordinates on a staggered grid using axially symmetric initial data, in first-order in time and first-order in space. The results of our experiment were successful, as indicated by the norm and pointwise convergence tests. We also attempted to evolve initial data in full 3D during the timeline of this project but didn't observe convergence in the appropriate norm – for that reason, they are omitted from this document.

7.2 Future work

Continuing work in the direction of treating future null infinity numerically, the next step is to evolve initial data in the absence of symmetries and show convergence. The generalization to full 3D implies that the fields g_ϕ and u_ϕ are no longer zero. Additional problems arise from this since the ϕ component of terms with the divergence of g_A and u_A on the 2-sphere have an additional factor of $\frac{1}{\sin^2 \theta}$, which diverges for $\theta = 0, \pi$.

Better results could be obtained by implementing the equations numerically using a non-staggered grid, thus avoiding extrapolation errors when computing the value of the fields at \mathcal{I}^+ . The difficulty of this is that the RHSs of the implemented equations can no longer have formally divergent terms, which we can surpass by applying the L'Hôpital rule on these terms. Furthermore, better grids should be included in NRPy+ in the near future so the treatment of the origin might be simpler in the future.

Only the model equations were solved numerically in this project. Although we expect similar results for the linearized GR equations that we derived (since they can be indeed modeled by the GU equations),

it would still be interesting to solve the linearized GR equations themselves, to verify and give more evidence of the correctness of our results. To do this, one would have to put together a careful match of the regularity conditions at the origin and at \mathcal{I}^+ . With this, all work for solving linearized GR on a flat background using hyperboloidal slices would be complete.

As mentioned in chapter 5, we could expand this work by linearizing around different backgrounds (for instance, Schwarzschild and Kerr). Essentially, that implies changing the background quantities in Eq. (5.10) and following the same steps taken here. In these backgrounds, additional complications may arise, for instance when relating the strong field region with the asymptotics. On the other hand, in some aspects evolving around these backgrounds might be simpler because, since we excise the BH interior, we do not have to deal with the origin.

Hyperboloidal evolution will be completely set up when all these results have been successfully generalized to full GR. Another field that needs to be included in the model is the *bad* field from the GBU model introduced in chapter 3. *Bad* fields are called “bad” because they decay slower than the others (their behavior grows with $\log(R)$).

There is good reason to believe that the hyperboloidal approach could be used in the future to obtain more accurate waveforms of GWs for binary BH simulations (in vacuum), thus contributing to better measurements of the properties of the sources. Finally, being able to introduce matter in these simulations in order to evolve neutron stars or accretion disks, with the advantage of being able to reach future null infinity, would be the last effort to have a complete approach. Since the hyperboloidal method is appropriate for extracting any signal traveling at the speed of light, we could also, in principle, extract electromagnetic waves at \mathcal{I}^+ .

Bibliography

- [1] D. Castelvechi and A. Witze, “Einstein’s gravitational waves found at last,” *Nature*, 2016. [Online]. Available: <https://doi.org/10.1038/nature.2016.19361>
- [2] B. P. Abbott *et al.*, “Observation of Gravitational Waves from a Binary Black Hole Merger,” *Phys. Rev. Lett.*, vol. 116, no. 6, p. 061102, 2016.
- [3] J. Sakstein and B. Jain, “Implications of the Neutron Star Merger GW170817 for Cosmological Scalar-Tensor Theories,” *Phys. Rev. Lett.*, vol. 119, no. 25, p. 251303, 2017.
- [4] A. Einstein, “The Foundation of the General Theory of Relativity,” *Annalen Phys.*, vol. 49, no. 7, pp. 769–822, 1916.
- [5] P. G. Ferreira, “Cosmological Tests of Gravity,” *Ann. Rev. Astron. Astrophys.*, vol. 57, pp. 335–374, 2019.
- [6] J. A. Wheeler, *A Journey into gravity and space-time*, 1990.
- [7] A. Ashtekar and B. Bonga, “On a basic conceptual confusion in gravitational radiation theory,” *Class. Quant. Grav.*, vol. 34, no. 20, p. 20LT01, 2017.
- [8] —, “On the ambiguity in the notion of transverse traceless modes of gravitational waves,” *Gen. Rel. Grav.*, vol. 49, no. 9, p. 122, 2017.
- [9] B. Bruegmann, J. A. Gonzalez, M. Hannam, S. Husa, U. Sperhake, and W. Tichy, “Calibration of Moving Puncture Simulations,” *Phys. Rev. D*, vol. 77, p. 024027, 2008.
- [10] C. Reisswig, N. T. Bishop, D. Pollney, and B. Szilagyi, “Characteristic extraction in numerical relativity: binary black hole merger waveforms at null infinity,” *Class. Quant. Grav.*, vol. 27, p. 075014, 2010.
- [11] N. T. Bishop and L. Rezzolla, “Extraction of gravitational waves in numerical relativity,” *Living Reviews in Relativity*, vol. 19, no. 1, p. 2, 2016. [Online]. Available: <https://doi.org/10.1007/s41114-016-0001-9>

- [12] N. T. Bishop, “Numerical relativity: combining the Cauchy and characteristic initial value problems.” in *Marcel Grossmann Meeting on General Relativity*, Jan. 1992, p. 1334.
- [13] T. Giannakopoulos, N. T. Bishop, D. Hilditch, D. Pollney, and M. Zilhao, “Gauge structure of the Einstein field equations in Bondi-like coordinates,” *Phys. Rev. D*, vol. 105, no. 8, p. 084055, 2022.
- [14] T. Giannakopoulos, D. Hilditch, and M. Zilhao, “Hyperbolicity of General Relativity in Bondi-like gauges,” *Phys. Rev. D*, vol. 102, no. 6, p. 064035, 2020.
- [15] A. Zenginoglu, “Hyperboloidal layers for hyperbolic equations on unbounded domains,” *J. Comput. Phys.*, vol. 230, pp. 2286–2302, 2011.
- [16] R. Penrose, “Asymptotic properties of fields and space-times,” *Phys. Rev. Lett.*, vol. 10, pp. 66–68, 1963.
- [17] H. Friedrich, “The asymptotic characteristic initial value problem for Einstein’s vacuum field equations as an initial value problem for a first order quasi-linear symmetric hyperbolic system,” *Proc. Roy. Soc. London*, vol. A 378, pp. 401–421, 1981.
- [18] S. G. Hahn and R. W. Lindquist, “The two-body problem in geometrodynamics,” *Annals of Physics*, vol. 29, no. 2, pp. 304–331, Sep. 1964.
- [19] F. Pretorius, “Evolution of binary black-hole spacetimes,” *Phys. Rev. Lett.*, vol. 95, p. 121101, Sep 2005. [Online]. Available: <https://link.aps.org/doi/10.1103/PhysRevLett.95.121101>
- [20] M. Duarte, J. Feng, E. Gasperin, and D. Hilditch, “High order asymptotic expansions of a good–bad–ugly wave equation,” *Class. Quant. Grav.*, vol. 38, no. 14, p. 145015, 2021.
- [21] M. Shibata, *Numerical Relativity*, 2016.
- [22] M. Alcubierre, *Introduction to 3+1 numerical relativity*, ser. International series of monographs on physics. Oxford: Oxford Univ. Press, 2008. [Online]. Available: <https://cds.cern.ch/record/1138167>
- [23] B. Gustafsson, H. Kreiss, and J. Oliger, *Time Dependent Problems and Difference Methods*, ser. A Wiley-Interscience Publication. Wiley, 1995. [Online]. Available: <https://books.google.pt/books?id=1JZ2mSQ-O6MC>
- [24] V. Mewes, Y. Zlochower, M. Campanelli, I. Ruchlin, Z. B. Etienne, and T. W. Baumgarte, “Numerical relativity in spherical coordinates with the Einstein Toolkit,” *Phys. Rev. D*, vol. 97, no. 8, p. 084059, 2018.
- [25] D. Hilditch, E. Harms, M. Bugner, H. Rüter, and B. Brügmann, “The evolution of hyperboloidal data with the dual foliation formalism: Mathematical analysis and wave equation tests,” *Class. Quant. Grav.*, vol. 35, no. 5, p. 055003, 2018.

- [26] E. Gasperin, S. Gautam, D. Hilditch, and A. Vañó Viñuales, “The Hyperboloidal Numerical Evolution of a Good-Bad-Ugly Wave Equation,” *Class. Quant. Grav.*, vol. 37, no. 3, p. 035006, 2020.
- [27] I. Ruchlin, Z. B. Etienne, and T. W. Baumgarte, “SENR/NRPy+: Numerical Relativity in Singular Curvilinear Coordinate Systems,” *Phys. Rev. D*, vol. 97, no. 6, p. 064036, 2018.
- [28] H.-O. Kreiss and J. Oliger, *Methods for the approximate solution of time dependent problems*. International Council of Scientific Unions, World Meteorological Organization, 1973, no. 10.
- [29] C. R. Evans, “A method for numerical simulation of gravitational collapse and gravitational radiation generation,” *Numerical Astrophysics*, p. 216, 1985.
- [30] C. Gundlach, J. M. Martin-Garcia, and D. Garfinkle, “Summation by parts methods for spherical harmonic decompositions of the wave equation in any dimensions,” *Class. Quant. Grav.*, vol. 30, p. 145003, 2013.
- [31] I. Suárez Fernández, R. Vicente, and D. Hilditch, “Semilinear wave model for critical collapse,” *Phys. Rev. D*, vol. 103, no. 4, p. 044016, 2021.
- [32] S. Gautam, A. Vañó Viñuales, D. Hilditch, and S. Bose, “Summation by Parts and Truncation Error Matching on Hyperboloidal Slices,” *Phys. Rev. D*, vol. 103, no. 8, p. 084045, 2021.



Geometric quantities

In this Appendix we give the explicit expressions of the metric components, which follow:

$$g^{00} = \frac{e^{-h_+} R^2 \dot{R}^{-2}}{\tau^2} \left(\cosh(h_\times) C_\theta^{-2} + \cosh(h_\times) C_\theta^{+2} + e^{2h_+} \cosh(h_\times) (C_\phi^- - C_\phi^+)^2 \right. \\ \left. + 2e^{h_+} C_\theta^+ (C_\phi^- - C_\phi^+) \sinh(h_\times) - 2C_\theta^- (\cosh(h_\times) C_\theta^+) + e^{h_+} (C_\phi^- - C_\phi^+) \sinh(h_\times) \right), \quad (\text{A.1})$$

$$g^{10} = \frac{e^{-h_+} R^2 \dot{R}^{-2}}{\tau^2} \left(\cosh(h_\times) (C_- C_\theta^{+2} + C_+ C_\theta^{-2}) + e^{2h_+} \cosh(h_\times) (C_\phi^- - C_\phi^+) (-C_\phi^+ C_- + C_\phi^- C_+) \right. \\ \left. + e^{h_+} C_\theta^+ \sinh(h_\times) (-2C_\phi^+ C_- + C_\phi^- (C_- + C_+)) + C_\theta^- (-\cosh(h_\times) C_\theta^+ (C_- + C_+) \right. \\ \left. + e^{h_+} \sinh(h_\times) (-2C_\phi^- C_+ + C_\phi^+ (C_- + C_+))) \right), \quad (\text{A.2})$$

$$g^{11} = \frac{e^{-h_+} R^2 \dot{R}^{-2}}{\tau^2} (\cosh(h_\times) C_\theta^{+2} C_-^{R2}) \quad (\text{A.3})$$

$$\begin{aligned}
& +e^{2h_+} \cosh(h_\times) C_\phi^{+2} C_-^{R2} - 2e^{h_+} C_\phi^+ (e^{h_+} \cosh(h_\times) C_\phi^- - C_\theta^- \sinh(h_\times)) C_-^R C_+^R \\
& + (\cosh(h_\times) C_\theta^{-2} + e^{2h_+} \cosh(h_+) C_\phi^{-2} - 2e^{h_+} C_\theta^- C_\phi^- \sinh(h_\times)) C_+^{R2} \\
& - 2C_\theta^+ C_-^R (e^{h_+} C_\phi^+ \sinh(h_\times) C_-^R + (\cosh(h_\times) C_\theta^- - e^{h_+} C_\phi^- \sinh(h_\times) C_+^R)) ,
\end{aligned}$$

$$g^{20} = -\frac{e^{-h_+} R \mathring{R}^{-2}}{\tau} \left(\cosh(h_\times) (C_\theta^+ - C_\theta^-) + e^{h_+} (C_\phi^- - C_\phi^+) \sinh(h_\times) \right) , \quad (\text{A.4})$$

$$g^{21} = -\frac{e^{-h_+} R \mathring{R}^{-2}}{\tau} \left(\cosh(h_\times) (C_\theta^+ C_-^R - C_\theta^- C_+^R) - e^{-h_+} \sinh(h_\times) (C_\phi^+ C_-^R - C_\phi^- C_+^R) \right) , \quad (\text{A.5})$$

$$g^{22} = e^{-h_+} \cosh(h_\times) \mathring{R}^{-2} , \quad (\text{A.6})$$

$$g^{30} = \frac{R \mathring{R}^{-2}}{\sin(\theta) \tau} \left(e^{h_+} \cosh(h_\times) (C_\phi^- - C_\phi^+) + (C_\theta^+ - C_\theta^-) \sinh(h_\times) \right) , \quad (\text{A.7})$$

$$g^{31} = -\frac{R \mathring{R}^{-2}}{\sin(\theta) \tau} \left(\sinh(h_\times) (C_\theta^- C_+^R - C_\theta^+ C_-^R) + e^{h_+} \cosh(h_\times) (C_\phi^+ C_-^R - C_\phi^- C_+^R) \right) , \quad (\text{A.8})$$

$$g^{32} = -\csc(\theta) \mathring{R}^{-2} \sinh(h_\times) , \quad (\text{A.9})$$

$$g^{33} = e^{h_+} \cosh(h_\times) \csc(\theta)^2 \mathring{R}^{-2} . \quad (\text{A.10})$$

The components of the linearized metric are given by

$$h_{00} = -\delta\varphi + \delta C_-^R - \delta C_+^R + \frac{1}{2}\tau , \quad (\text{A.11})$$

$$h_{10} = -\frac{\delta C_+^R + \delta C_-^R}{2} , \quad (\text{A.12})$$

$$h_{11} = \delta\varphi - \frac{\tau}{2}, \quad (\text{A.13})$$

$$h_{20} = \frac{R}{2}(\delta C_\theta^- - \delta C_\theta^+), \quad (\text{A.14})$$

$$h_{21} = -\frac{R}{2}(\delta C_\theta^- + \delta C_\theta^+), \quad (\text{A.15})$$

$$h_{22} = R^2(\delta h_+ - 2R\dot{R}^{-1}), \quad (\text{A.16})$$

$$h_{30} = \frac{R \sin(\theta)}{2}(\delta C_\phi^- - \delta C_\phi^+), \quad (\text{A.17})$$

$$h_{31} = -\frac{R \sin(\theta)}{2}(\delta C_\phi^- + \delta C_\phi^+), \quad (\text{A.18})$$

$$h_{32} = R^2 \sin(\theta) \delta h_\times, \quad (\text{A.19})$$

$$h_{33} = -R^2 \sin(\theta)^2 (2R\dot{R}^{-1} + \delta h_+). \quad (\text{A.20})$$

The components of \bar{h} , as defined in chapter 2, are

$$\bar{h}_{00} = -2R\dot{R}^{-1} - \frac{\tau}{2}, \quad (\text{A.21})$$

$$\bar{h}_{10} = -\frac{\delta C_+^R + \delta C_-^R}{2}, \quad (\text{A.22})$$

$$\bar{h}_{11} = 2R\dot{R}^{-1} - \frac{\delta C_-^R - \delta C_+^R}{2}, \quad (\text{A.23})$$

$$\bar{h}_{20} = \frac{R}{2}(\delta C_\theta^- - \delta C_\theta^+), \quad (\text{A.24})$$

$$\bar{h}_{21} = -\frac{R}{2}(\delta C_\theta^- + \delta C_\theta^+), \quad (\text{A.25})$$

$$\bar{h}_{22} = R^2(\delta h_+ - \delta\varphi), \quad (\text{A.26})$$

$$\bar{h}_{30} = \frac{R \sin(\theta)}{2}(\delta C_\phi^- - \delta C_\phi^+), \quad (\text{A.27})$$

$$\bar{h}_{31} = -\frac{R \sin(\theta)}{2}(\delta C_\phi^- + \delta C_\phi^+), \quad (\text{A.28})$$

$$\bar{h}_{32} = R^2 \sin(\theta) \delta h_\times, \quad (\text{A.29})$$

$$\bar{h}_{33} = -R^2 \sin(\theta)^2 (\delta\varphi + \delta h_+). \quad (\text{A.30})$$

B

Source terms in the GU model

Using the same notation as in chapter 5.3, the source terms in equations (5.37) and (5.38), as well as in (6.4), are given by

$$S_{G^+} = -\frac{\chi^2 S_g}{1+H'} - \frac{R' c_-^r}{R\chi} (R-\chi)(R+\chi)G^- + \frac{2R' c_-^r}{\chi^2} (\chi - R\chi')G + \frac{R' c_-^r}{R\chi} (2R\chi' - \chi)G^+, \quad (\text{B.1})$$

$$S_{G^-} = -\frac{\chi S_g}{1-H'} + \frac{R' c_+^r}{R\chi} G^+ + \frac{R' c_+^r}{R\chi} (R\chi' - \chi)G^- - \frac{R' c_+^r}{\chi^2} G, \quad (\text{B.2})$$

$$S_{U^+} = -\frac{\chi^2 S_u}{1+H'} + \frac{R' c_-^r}{R\chi} (\chi - R)(2R + \chi)U^- + \frac{2R' c_-^r}{\chi^2} (2\chi - R - 2R\chi')U \quad (\text{B.3})$$

$$+ \frac{R'}{R\chi c_-^r} (R - \chi + 3R\chi')U^+, \quad (\text{B.4})$$

$$S_{U^-} = \frac{\chi S_u}{-1+H'} + \frac{2R' c_+^r}{\chi^3} (R - \chi)U - \frac{R'}{R\chi^2 c_+^r} (R - \chi)U^+ - \frac{R' c_+^r}{R\chi} (R + \chi - 2R\chi')U^-. \quad (\text{B.5})$$

